geosciences

MDPI

Article

Aeolian Dust Preserved in the Guliya Ice Cap (Northwestern Tibet): A Promising Paleo-Environmental Messenger

Emilie Beaudon [1,*], Julia M. Sheets [2,3], Ellen Martin [4], M. Roxana Sierra-Hernández [1], Ellen Mosley-Thompson [1,5] and Lonnie G. Thompson [1,3]

[1] Byrd Polar and Climate Research Center, The Ohio State University, Columbus, OH 43210, USA
[2] Subsurface Energy Materials Characterization and Analysis Laboratory (SEMCAL), Columbus, OH 43210, USA
[3] School of Earth Sciences, The Ohio State University, Columbus, OH 43210, USA
[4] Department of Geological Sciences, University of Florida, Gainesville, FL 32611, USA
[5] Department of Geography, The Ohio State University, Columbus, OH 43210, USA
* Correspondence: beaudon.1@osu.edu

Abstract: Asian aeolian dust is a primary factor in Northern Hemisphere atmospheric dynamics. Predicting past and future changes in atmospheric circulation patterns relies in part on sound knowledge of Central Asian dust properties and the dust cycle. Unfortunately for that region, data are too sparse to constrain the variation in dust composition over time. Here, we evaluate the potential of a Tibetan ice core to provide a comprehensive paleo-atmospheric dust record and thereby reduce uncertainties regarding mineral aerosols' feedback on the climate system. We present the first datasets of the mineralogical, geochemical, and Sr-Nd isotope composition of aeolian dust preserved in pre-Holocene layers of two ice cores from the Guliya ice cap (Kunlun Mountains). The composition of samples from the Summit (GS; 6710 m a.s.l.) and Plateau (GP; 6200 m a.s.l.) cores reveals that the characteristics of the dust in the cores' deepest ice layers are significantly different. The deepest GS layers reveal isotopic values that correspond to aeolian particles from the Taklimakan desert, contain a mix of fine and coarse grains, and include weathering-sensitive material suggestive of a dry climate at the source. The deep GP layers primarily consist of unusual nodules of well size-sorted grey clay enriched in weathering-resistant minerals and elements typically found in geothermal waters, suggesting that the dust preserved in the oldest GP layers originates from a wet and possibly anoxic source. The variability of the dust composition highlighted here attests to its relevance as a paleo-environmental messenger and warrants further exploration of the particularly heterogenous Guliya glacial dust archive.

Keywords: Tibetan ice core; aeolian dust; Sr-Nd isotopes; trace elements; clay; loess; weathering; provenance

check for updates

Citation: Beaudon, E.; Sheets, J.M.; Martin, E.; Sierra-Hernández, M.R.; Mosley-Thompson, E.; Thompson, L.G. Aeolian Dust Preserved in the Guliya Ice Cap (Northwestern Tibet): A Promising Paleo-Environmental Messenger. *Geosciences* **2022**, *12*, 366. https://doi.org/10.3390/geosciences12100366

Academic Editors: Roveri Marco and Jesus Martinez-Frias

Received: 15 July 2022
Accepted: 26 September 2022
Published: 30 September 2022

1. Introduction

Airborne mineral dust (i.e., microparticles) has the largest mass emission rate of all aerosol types [1] and constitutes 70% of the global aerosol mass burden [2]. Dust particles, emitted by aeolian erosion of arid and semi-arid soils, affect the physical and chemical properties of the atmosphere, thereby influencing Earth's climate system [3]. Aeolian microparticles change the atmospheric radiation balance through their absorption and scattering properties, modify cloud microphysics by acting as condensation nuclei, influence marine biochemistry and oceanic uptake of atmospheric CO_2, fertilize terrestrial ecosystems, and impact atmospheric chemistry. All of these processes are directly linked to the particles' size, morphology, geochemical and mineralogical composition, and their atmospheric transport pathways. In turn, the parameters controlling mineral dust emissions (i.e., aridity, vegetation and snow cover, soil types, wind velocity, precipitation, and topographic features) are very sensitive to climate variations [4] and involve feedbacks that are recognized as major uncertainties of climate change [5].

Characterizing mineralogical and geochemical fingerprints of aeolian dust and determining their change through time enables the extraction of paleo-environmental and paleo-synoptic information from aeolian deposits, and thereby reduces uncertainty regarding the role of dust in the climate cycle. However, despite the valuable paleo-environmental message carried by aeolian dust, paleo-dust records remain globally scarce and underexplored [6]. Surprisingly, a paleo-dust record is also lacking in NW Tibet, one of the largest atmospheric dust source regions in the Northern Hemisphere. This research provides the first mineralogical and geochemical information on aeolian microparticles deposited on the Guliya ice cap (NW Tibet) during the Late Pleistocene and demonstrates the paleo-environmental value that paleo-dust records extracted from the Guliya ice cores likely hold.

Ice cores are commonly used as terrestrial archives of past atmospheric microparticle deposition (e.g., [7]). Based on the principle that the particle size at the deposition site becomes finer with distance from the source, the source-to-sink relative distance, paleo-winds strength, and aridity are inferred from the particles' size and concentration, as measured in ice. In polar ice, for instance, the concentration of microparticles is much higher during glacial than interglacial periods [8–10]. However, this is not always the case in tropical ice cores. For example, lower dust concentration in the Sajama (Bolivia) core for the last glacial period reflects the wetter conditions and a more extensive snow cover [11]. Not only do the particles' physical properties reflect past atmospheric dynamics and hydroclimate; the mineralogical, isotopic, and elemental composition of the dust provide environmental information regarding the source of windborne material. Physical and geochemical characteristics thereby complement each other in constraining the geographical source of the dust, its distance to the deposition site and the atmospheric transport conditions (e.g., wind strength).

Trace element (TE) ratios and rare earth element (REE) abundances and distribution patterns are other source-specific parameters of mineral particles that can be conserved during long-range windborne transport. REEs are particularly well suited for investigating mineral aerosol characteristics that are controlled by provenance and pedogenetic processes [12–14]. Because their variability results from changes in the mineral composition of aeolian dust [15], elemental ratios complement the panel of geochemical tools as diagnostic source tracers.

The combination of strontium (^{87}Sr/^{86}Sr) and neodymium (^{143}Nd/^{144}Nd) isotopic ratios is another powerful source-area fingerprint for dust as these ratios depend on the isotopic composition and age of the rock from which they are derived [16–23]. The isotopic compositions of the ice core dust samples compared to those of Potential Source Areas (PSA) samples indicate variations in the mineral aerosols' geographical provenance, which may be used to resolve past climate changes [17,24,25]. For example, the first investigations of the isotopic fingerprint of airborne dust from ice cores suggested that Greenland is influenced by proximal sources during warm periods and by remote Asian sources (e.g., the Gobi Desert) in colder periods [26,27], until subsequent studies excluded the Gobi Desert as a potential dust source [28]. The most recent and extensive investigations of the main Greenland dust sources during glacial periods support the Taklimakan and Tengger deserts, and to a lesser extent Central Europe as the more likely contributors [29–31]. On a seasonal scale, the dust source fluctuation between the Taklimakan desert in spring and Inner Mongolia in autumn is linked to the Arctic Oscillation phase and to the position of the Westerly jet. Various studies [22,32,33] provided new evidence of a latitudinal gradient in the Sr and Nd isotopic composition of cryoconite, and snowpack dust collected on five glaciers of the northeast Tibetan Plateau (TP), from which they infer dust atmospheric transport pathways. On an event-based time scale, aeolian dust from the Gobi Desert and the Chinese Loess Plateau (CLP) was also identified by its Sr-Nd isotopic signature in the snow of Mt. St. Elias (Yukon Territory, Canada), following a dust storm event that occurred in Asia and was transported across the North Pacific Ocean by clouds [34].

High elevation glaciers on the TP, dominating one of Earth's most arid regions, are repositories of tropospheric microparticles that have experienced mixing and gravitational sorting during transport. Even though local (i.e., coarser grain size fraction) soil dust is a non-negligible source, the particles entrapped in these high-altitude ice fields are substantially sorted by grain size with longer range transport enhancing sorting, making long range transported dust a prevalent deposit on TP glaciers [33,35]. The major dust storm events, during which particles rise above the boundary layer and are then transported for thousands of kilometers, are most important to climate systems. Therefore, the high altitude Guliya ice cap (western Kunlun Mountains, 35.12 to 35.22° N, 81.23 to 81.35° E; maximum elevation: 6710 m a.s.l.; Figure 1) situated between the 400 to 470 hPa pressure levels in the Westerlies, represents a favorable deposition site for dust transported long distances by large storms.

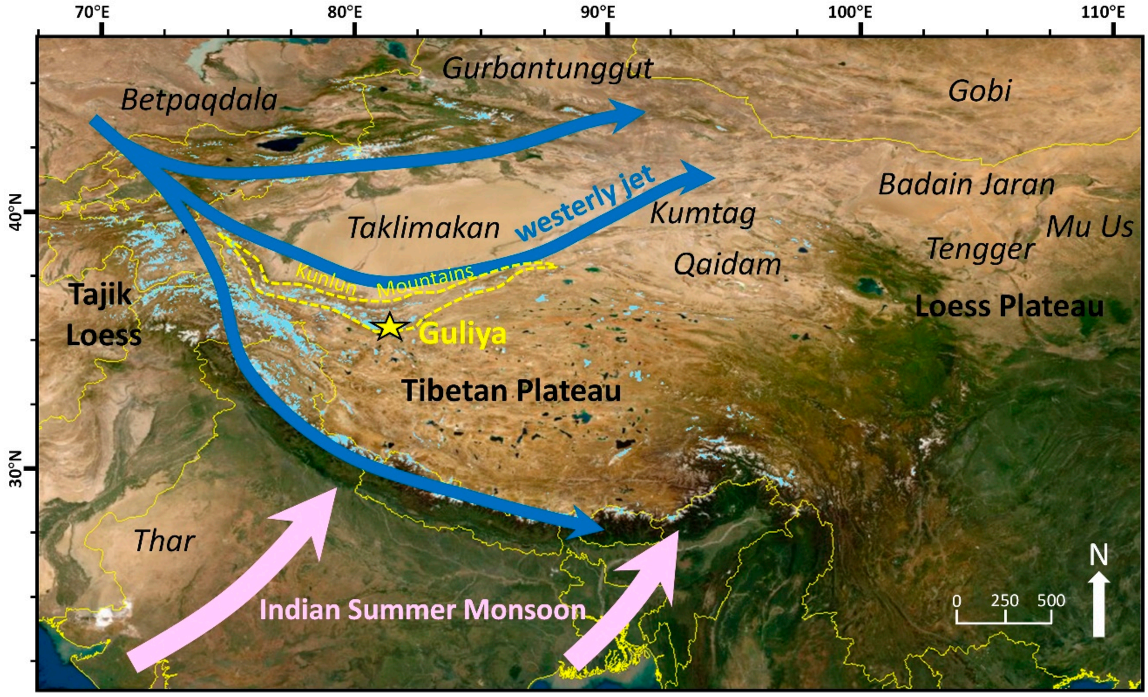

Figure 1. Third Pole region with the location of the Guliya ice cap (yellow star) in the Kunlun Mountains (yellow dashed line), the main deserts and loess sub-regions. The arrows depict the trajectories of the main seasonal air masses that influence NW Tibet climate. (Source background image: ESRI, world imagery).

A growing body of research has characterized the Sr-Nd isotopic signature of Chinese [26,31,36–38] and Indian [39,40] deserts' aeolian material, making it possible to identify Asian sub-regions, or desert sources, of dust preserved in Tibetan glaciers. The remote continental location of Tibetan glaciers ensures that the marine influence on their dust Sr-Nd isotopic composition is negligible compared to that of polar ice sheets [22]. However, riverine and lacustrine contributions to the Sr isotopic composition of glacial dust remains possible through the deposition of carbonate from paleo-lacustrine sediments onto the glaciers [41,42]. These evaporitic minerals containing calcium carbonate ($CaCO_3$) have lower $^{87}Sr/^{86}Sr$ ratios than those associated with aluminosilicates and can impede the accurate isotopic fingerprinting of the dust source. For this reason, the carbonate fraction is commonly removed from the ice core insoluble mineral dust by weak acid leaching. Despite their potential as archives of Asian dust provenance, to date, only three shallow ice cores from the Tibetan Plateau (Dunde ice cap, [35]), Tien Shan (Miaoergou glacier, [43]) and the Himalaya (East Rongbuk glacier, [44]), referred to collectively as the Third Pole region, have been analyzed for Sr and Nd isotopes. Other Third Pole glacier dust provenance studies using TEs and REEs have been conducted on surface snow or samples from shallow ice cores, and thus provide information on modern aerosols only [33,35,43–50]. A deeper temporal perspective on aeolian dust composition and source is lacking for Tibet, especially in the northwestern regions. The first geochemical investigation of a Central Asian ice core was conducted by [45] on a shallow core from Inilcheck glacier in Tien Shan (Kyrgyzstan), which was found to accumulate loess during deposition events. Calcite and gypsum originating from various sites constituted the average background mineralogical composition of Inilcheck dust. Ref. [35] examined the isotopic signature in discrete samples from a shallow ice core from the Dunde ice cap (Qilian Mountains, Northern China) and found ^{87}Sr/^{86}Sr and ε_{Nd} values within the same range as those of the Taklimakan and Qaidam sands. They conclude that, under the present climate, Dunde dust originates from the Tarim and the Qaidam Basins, where it is entrained and transported over long distances by westerly winds. Similarly, for the Miaoergou glacier (Tien Shan, north of Tarim Basin), an isotopic investigation was conducted on six discrete contemporary ice core samples (dated between 1956 to 2000 AD) and conclusions were drawn from a relatively short time interval [43]. Using REE and Sr-Nd isotopes, these authors documented that since 1956 AD the Taklimakan and the Gobi deserts were the main sources of aeolian dust deposited on Miaoergou. These findings were corroborated by [33] using the Sr and Nd isotopic compositions of dust from cryoconites at the surface of Miaoergou glacier.

In this study, the mineralogical, elemental, and radiogenic isotopic signatures of the aeolian dust sampled from discrete deep sections of two ice cores (retrieved from the Summit and Plateau sites) from the Guliya ice cap are characterized to assess their potential in tracing the long-term variability of paleo-hydro-climatic conditions prevailing in NW Tibet, and to identify the lithological and geographical source area(s) for the dust. The sampling approach was guided by visual characteristics of dust in the ice (e.g., color, layer feature, orientation). We also investigated discrete dust samples in ice sections preceding and succeeding several stadial/interstadial transitions (i.e., the cold/warm transitions within the Last Glacial Period) recorded in the 1992 Guliya ice core [11], for which we expect to observe a pronounced variability in the dust parameters. The results are interpreted considering the compositions of aeolian deposits discussed in the literature.

2. Study Site, Materials, and Methods

2.1. The Guliya Ice Cap and Surrounding Deserts

The Guliya ice cap is a ~200 km^2 ice field located in the Kunlun Mountains and situated under the atmospheric dominance of the continental westerly flow which is particularly intense during winter (Figure 1). Indian Summer Monsoon incursions can occasionally and indirectly modulate the atmospheric circulation pattern over NW Tibet (Figure 1). This location makes the Guliya site particularly relevant for the study of the Westerlies' intensity, which can entrain and transport mineral aerosols from northern (e.g., Gurbantünggüt, Taklimakan) and western deserts (e.g., Tajik loess desert) to the very high-altitude surface of the glaciers in the region and to the free troposphere (>6000 m a.s.l.). Ultimately, transport can be achieved over long distances to Eastern China and the remote Pacific region [51,52]. Additionally, with the influence of the Indian Summer Monsoon and a more southwestern circulation during warmer periods, the Guliya ice cap could potentially be the sink for mineral dust transported from the sandy Sahara, the Arabian Peninsula, the Thar Desert in Rajasthan [39,40], and the southern TP.

The Kunlun Mountains ring the southern edge of the Taklimakan sandy desert in the Tarim Basin and circumscribe the arid northwestern TP region. Moraines and loess deposits are present on the northern slopes of the Kunlun Mountains and represent a proximal source of mineral aerosols to the Guliya glacier. The loess deposits in the Kunlun Mountains are among the highest in the world. They are derived from the Taklimakan Desert dust entrained by surface northeasterly winds and deposited on the windward slopes of the Kunlun Mountains [52]. Tibetan Plateau soils and Quaternary deposits (e.g., talus fans, alluvial fans, and paleo-lake beds) on the southern side of the Kunlun Mountains also represent potential sources of aeolian silt particles to the Guliya ice cap [53]. The vast desert areas surrounding the Guliya ice cap and the very low snow accumulation on the ice cap (230 mm w.e. yr^{-1} at the Plateau site, [54]) favor very high dust concentrations in the Guliya ice core (1650–1992 A.D. median dust concentration = 194 × 10^3 particles mL^{-1}, [55]). The high dust content of the core presents a great advantage in terms of sampling resolution for geochemistry as compared to cleaner polar ice cores for which more voluminous ice samples are required to collect a sufficient mass of insoluble material for the Sr and Nd isotope measurements (typically 200 ng for Sr and 50 ng for Nd). Arid conditions at the Summit of the Guliya ice cap are further exacerbated by very low snow precipitation relative to sublimation. The average annual ice layer thickness at the Summit (125 mm ice eq. yr^{-1}) is less than half of that on the Plateau (262 mm ice eq. yr^{-1}), a lower site on the ice cap [54].

2.2. The Guliya Ice Cores

2.2.1. Chronology

In 2015, three ice cores, each ~51 m in length, were recovered to bedrock from the Guliya Summit (6710 m a.s.l.), and two longer cores, one to bedrock (~310 m), were recovered from the Plateau (6200 m a.s.l.) by the Ice Core Paleoclimatology Research Group (ICPRG) of the Byrd Polar and Climate Research Center (BPCRC, The Ohio State University (OSU)) in partnership with the Institute of Tibetan Plateau Research (China). All ice cores are extracted in sections of ~1 m length by ~10 cm diameter. Here, our primary analytical effort involves two of the five ice cores: a Summit core (35°17.37′ N; 81°29.73′ E, 6710 m a.s.l., hereafter GS) and the deeper Plateau core (35°13.98′ N; 81°28.1′ E, 6200 a.s.l.; hereafter GP) which both reached bedrock. ^{36}Cl data from a deep ice core extracted from the Plateau site in 1992 suggest that the deepest 20 m of GP may be older than 500 kyr [11]. If correct, GP would be the oldest ice core archive yet recovered from the mid-latitudes.

The top 110 kyr, which is the better chronologically constrained part of the GP core, is the only mid-latitude climate archive comparable to the deep Greenland and Antarctic ice cores in terms of age, dating precision, and diversity of paleo-environmental information [56,57]. For instance, the $\delta^{18}O$ curve of the 1992 Plateau core indicates that temperature fluctuations during the last 110 kyr (Figure 2) were consistent with glacial cycles recorded in Northern Hemisphere ice cores and North Atlantic Ocean sediments [11,58,59]. The chronology of the 2015 GS core also is under development, the discussion of which is beyond the scope of this paper. However, to provide some context to the work presented here, we note that the bottom layers of GS extend into the deglaciation (~16 kyr). The paleo-environmental interpretation of the GP and GS dust geochemistry presented here does not take the sample's age into consideration. For this reason, and despite the reliable original timescale developed for the upper 200 m of the 1992 GP core [11], the results of this study are discussed in terms of sample depth rather than sample age (Figure 2).

2.2.2. Stratigraphic Observations

During the processing of the ice core sections in the freezer facilities of the BPCRC, a stratigraphic description of GS and GP allowed the distinction of different types of dust within both ice cores. The most illustrative example is a progressive transition with depth from the light brown silt-sized particles to the grey nodules dominating the bottom 20 m of GP core. Both types of dust are observed in ice layers around 300 m depth (Figure A1). These prominent features in the ice core stratigraphy suggest that the source area for dust, the transport pathways of mineral aerosols, the climate at the dust source, or englacial conditions, have changed markedly over the time period represented by the Guliya ice cores. This was explored further by characterizing mineralogical, elemental (TE and REE), and Sr-Nd isotopic signatures, and thus aiding the identification of the geographical source(s) of the different types of dust deposited on the Guliya ice cap. For the GS core, the deeper layers with more dust layers visible were a natural first choice for sampling and allowed a preliminary comparison of the bottom ice layers at the two sites (Summit and Plateau).

2.3. Sample Preparation and Analysis

Two types of samples are used in this study from both GP and GS: **(1)** dust particles collected on filters from melted ~1 m ice core sections, hereafter referred to as "dust filters"

(Section 2.3.1), and **(2)** acid-leached ice core subsamples from ~1 m ice sections, hereafter referred to as "ice samples" (Section 2.3.2) (Figure A2). Subsamples refer to the ~2 to 10 cm long individual ice pieces cut along depth from each ~1 m long ice sections (Table 1).

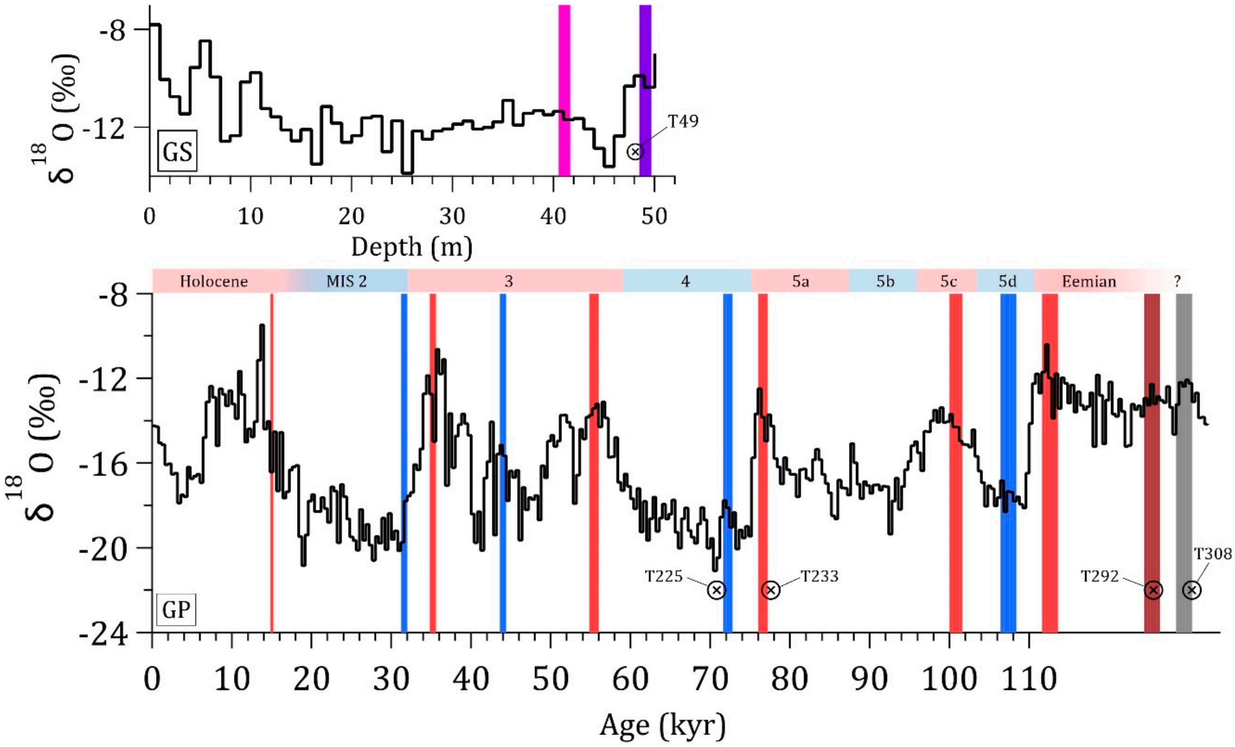

Figure 2. 5 m-averaged $\delta^{18}O$ record vs. depth of the Guliya 2015 Summit core (GS) (upper panel); $\delta^{18}O$ time series of the 1992 Plateau core [11] illustrating the climatic periods recorded in the Guliya Plateau (GP) ice core (lower panel) as defined by [11]. The vertical bars mark the 1 m ice core sections sampled for microparticle concentration and size, and trace element concentrations in ice corresponding to "warm" (purple/red) or "cold" (pink/blue) periods. The bars are increasingly wider with age (and depth) as 1 m of ice comprises more time toward the bottom of the glacier due to the increased thinning of successive ice layers with depth. Note that the vertical bars representing T290 and T292 (brown), and T305 and T306 (grey) are juxtaposed and therefore appear as two bars instead of four on the time axis. The crossed circles indicate the depth at which dust filtrate from 1 m ice sections were collected on filters (i.e., dust filter samples) for geochemical and isotopic analyses (see Table 1).

Five dust filters (4 from GP and 1 from GS), and sixteen ice samples (14 from GP and 2 from GS) were selected for elemental geochemistry analysis (Table 1, Figure 2). The GP samples range in age from the Holocene to the Eemian (and possibly older). The bulk $^{87}Sr/^{86}Sr$ and $^{143}Nd/^{144}Nd$ isotopic compositions of these five dust filters were determined to constrain the geographical source of the brown and the grey dust observed at different depths of GS and GP. Two additional dust filters (T50 from GS and T309 from GP, Table 1) were analyzed for bulk mineralogy only, to also help elucidate provenance. It is important to note that for this preliminary study, collecting a sufficient amount of insoluble material and being able to readily compare the Guliya samples to those from the Dunde ice cap (then the only other Tibetan ice core dust analyzed for Sr-Nd isotopes [35]) were two primary concerns. Consequently, dust has not been treated with any acid to remove the carbonate fraction, nor has it been size-sorted to target the clay-size fraction. Therefore, the results discussed here represent the bulk of the dust collected on filters.

Table 1. Sampling and analytical information.

Core Site	Sample ID (n Subsamples)	Depth (m)	Age (kyr)	Dust Extraction Method	Dust Color	1m-Section Mean δ^{18}O (‰)	Mineralogy	Geochemistry (TE, REE *)	^{87}Sr/^{86}Sr ^{143}Nd/^{144}Nd
Fiters (>0.22 μm bulk size faction)									
Summit (GS)	T49	47.7–48.6	~16	Filtration	brown	−10.5	-	ICPMS *	MC-ICPMS
	T50	48.6–49.5	~16	Filtration	brown	−10.9	XRD SEM-EDXS		
Plateau (GP)	T225	223.3–224.3	~70	Filtration	-	−19.4	-	ICPMS *	MC-ICPMS
	T233	231.5–232.5	~77	Filtration	-	−15	-	ICPMS *	MC-ICPMS
	T292	290.2–291.2	>110	Filtration	brown	−12.9	-	ICPMS *	MC-ICPMS
	T308	305.5–306.4	>110	Filtration	grey	−13	-	ICPMS *	MC-ICPMS
	T309	306.4–307.5	>110	Filtration	grey	−12.9	XRD SEM-EDXS		
Ice samples (<2 μm size fraction)									
Summit (GS)	T41(11)	40.1–41.1	~16	Acid leaching	-	−11.4		ICP-SF-MS	
	T50 (10)	48.6–49.5	~16	Acid leaching	brown	−10.9		ICP-SF-MS	
Plateau (GP)	T136 (9)	136.3–137.2	~15	Acid leaching	-	−13.2		ICP-SF-MS	
	T173 (9)	173.1–174.1	~32	Acid leaching	-	−18.9		ICP-SF-MS	
	T181 (7)	180.9–181.9	~35	Acid leaching	-	−12.7		ICP-SF-MS	
	T197 (5)	196.3–197.1	~44	Acid leaching	-	−16.1		ICP-SF-MS	
	T209 (7)	207.3–208.3	~55	Acid leaching	-	−12.5		ICP-SF-MS	
	T227 (8)	225.3–226.3	~72	Acid leaching	-	−18.7		ICP-SF-MS	
	T232 (9)	230.4–231.5	~76	Acid leaching	-	−13		ICP-SF-MS	
	T262 (9]	260.4–261.3	~101	Acid leaching	-	−13.7		ICP-SF-MS	
	T273 (9)	271.2–272.2	~107	Acid leaching	-	−18.2		ICP-SF-MS	
	T278 (10)	276.2–277.3	>110	Acid leaching	-	−13.8		ICP-SF-MS	
	T290 (16)	288.3–289.3	>110	Acid leaching	brown	−13.5		ICP-SF-MS	
	T292 (16)	290.2–291.2	>110	Acid leaching	brown	−12.9		ICP-SF-MS	
	T305 (17)	302.4–303.4	>110	Acid leaching	brown & grey	−13.4		ICP-SF-MS	
	T306 (16)	303.4–304.4	>110	Acid leaching	grey	−13.6		ICP-SF-MS	

* samples analyzed for REE with ICPMS.

The entire GS and GP ice cores, including the ice samples used for this study, were previously analyzed for oxygen isotopes ($\delta^{18}O$), major ions, and insoluble microparticles (size and concentration) in the ICPRG's Class 100 Clean Room. However, the full sample resolution records of these data will not be presented in this manuscript. Measurements of particle size distribution and concentration were performed with a Multisizer IV © Coulter counter (aperture diameter: 30 µm; 14 size bins: 0.63 to 16 µm, [54]) on diluted aliquots of melted ice samples. Note that each dust filter and ice sample ID number (T-XXX) refers to the cylinder (or "Tube") in which the corresponding ~1 m ice section was stored following extraction from the glacier. Therefore, the sample ID number is similar, but not identical to, the sample's average depth (Table 1).

2.3.1. Dust Filters

A diluted portion of the melted ice samples was consumed by the Coulter counter analyses [54]. From the remaining undiluted portion, particles were filtered onto a cellulose Millipore filter (pore diameter 0.22 µm), stored in a Petri dish, and each filter was kept in the Class 100 clean room until analysis. Each filter collected the bulk fraction (>0.22 µm) of insoluble material contained in 1 m of ice core. The different types and colors of dust observed in the layers of the ice cores could still be visually distinguished among the filters (Figure A1 and [60] there in). Although the ages of the samples are not considered in this study, it is important to note that the increased layer thinning with depth makes one meter of ice comprise a longer time period as it is sampled deeper along the core. Conversely, in the upper part of the ice cores, time is relatively more stretched, making transitions between dust types more "diluted" in time, and thus less conspicuous. In this preliminary study, the four dust filters from GP correspond to top depths (m) of 223 (T225), 232 (T233), 290 (T292) and 305 (T308), and the dust filter from the GS core corresponds to 48 m depth (T49) (Table 1, Figure 2).

Mineralogy

The two additional dust filters, T50 from GS and T309 from GP were first analyzed directly using powder X-ray diffraction (XRD) to determine qualitative bulk mineralogy of all grain sizes present in the samples. Filter mounts were prepared by adhering them with double-sided adhesive tape to glass slides and mounting the slides onto XRD sample holders. Small portions of each filter were used to prepare samples for scanning electron microscopy and energy dispersive X-ray spectroscopy (SEM-EDXS) by pressing aluminum stubs with carbon adhesive tape directly onto the filter samples. These first steps are important for identifying trace minerals in the filters that may be sensitive to water or alcohol washing, which are required for the separation of grains that include only the aeolian size fraction of material transported to the Guliya ice cap. Because the filter mounts produced a high background in XRD scans that made data interpretation difficult, a second set of mounts were prepared by isopropyl washing of dust from the filters onto zero-background holders. The resulting XRD scans from this second sample preparation method yielded better results (see Section 3.1.3). XRD allows identification of major and minor minerals present, while SEM-EDXS yields complementary micro-analytical data to support mineral identification by XRD, to detect trace minerals, and to provide morphological information. Particular attention was focused on the clay minerals (commonly found within the fine fraction, <2 µm) which tend to adsorb trace metals (e.g., [61]).

Sr-Nd Isotope and Elemental Geochemistry Analysis by MC-ICPMS and ICPMS

Particulates were remobilized from each dust filter and then centrifuged in a conical tube with ultrapure water. After centrifugation (30 min), the clear supernatant was discarded using a syringe, and the remaining water was evaporated in a class 100 laminar flow box. Extracted particles were dissolved in an HF–HNO_3 mixture in Teflon hexvials that were heated to 100–120 °C for three days. The full acid digestion allows the determination of total elemental concentrate ons in the dust filter samples (contrary to a fraction of the total TEs determined by acid leaching of ice samples (see Section 2.3.2)). Following sample dissolution, Sr and REEs were isolated on 3 mL quartz columns using conventional ion-exchange chromatography primary columns packed with AG 50 W-X12 (200–400 mesh) resin. Strontium was extracted with 3.5 N HCl and the REE fraction was collected in 6 N HCl. Neodymium (Nd) was then separated from the other REEs on Teflon columns using 800 μL of LnSpec resin as the cation exchange medium. The Sr-Nd isotopes were analyzed on a Nu Plasma Multi-Collector Inductively Coupled Plasma Mass Spectrometer (MC-ICPMS) at the University of Florida (UF). Sr isotopes were analyzed using wet plasma and the time resolved analysis (TRA) method developed by [62]. The long-term average $^{87}Sr/^{86}Sr$ value of TRA-measurements of NIST 987 (reference value: $^{87}Sr/^{86}Sr = 0.710248$, [63]) at UF is 0.710244 (± 0.000024, 2σ) and was used to normalize the measured data. Procedural blanks were less than 100 pg Sr or four orders of magnitude less than sample concentrations. Samples for Nd isotopic analyses were also analyzed using the TRA method. Samples were aspirated through a DSN-10 desolvating nebulizer system. The average of measured $^{143}Nd/^{144}Nd$ ratios for the standard JNdi-1 (reference value: $^{143}Nd/^{144}Nd = 0.512115$, [64]) is 0.512115 ($\pm 0.000014$, 2σ) and was used to normalize the $^{143}Nd/^{144}Nd$ isotopic ratios of samples. The long-term 2σ external reproducibility of JNdi-1 analyses (± 0.000014) is equivalent to ± 0.27 ε_{Nd} units, where ε_{Nd} is calculated using the equation:

$$\varepsilon_{Nd}\,(0) = ((^{143}Nd/^{144}Nd)_{sample}/(^{143}Nd/^{144}Nd)_{CHUR} - 1) \times 10000 \quad (1)$$

and the isotopic composition of the Chondritic Uniform Reservoir (CHUR) is $(^{143}Nd/^{144}Nd)_{CHUR} = 0.512638$ [65]. Procedural blanks were approximately 15 pg Nd or four orders of magnitude less than sample concentrations.

The determination of the geochemical composition of the dust filters also entailed the analysis of 19 TEs (Li, Ti, V, Cr, Co, Ni, Cu, Zn, Ga, Rb, Sr, Zr, Nb, Cs, Ba, Nd, Ta, Pb, U) and 16 REEs (La, Ce, Pr, Nd, Sm, Eu, Gd, Tb, Dy, Ho, Er, Tm, Yb, Lu) including Sc and Y on a Thermo Scientific Element 2 ICPMS. Samples were diluted 1:1 with 5% HNO_3 spiked with 8 parts per billion (ppb) rhenium (Re) and rhodium (Rh) and analyzed using in-house standards. Long-term measurement reproducibility was checked against the AGV1 standard. Relative standard error between repeated measurements of AGV1 was less than 8% for all elements.

2.3.2. Ice Samples

The 16 selected ice samples (two from GS and 14 from GP) were cut into a total of 158 subsamples (5 to 10 cm long) with a carbon steel band saw and were transferred to a Class 100 clean room where they were decontaminated by triple washing with ultra-pure water. The ice samples were melted at room temperature in pre-cleaned LDPE containers and acidified with ultra-pure HNO_3 (optima grade) to a final concentration of 2% (*v/v*). Following acidification, the samples were kept in the clean room for 30 days to allow the complete leaching of TEs by the acid, which releases a fraction of the total TEs in the sample [66]. The subsequent analysis by ICPMS (Thermo Scientific Element 2 housed at BPCRC) coupled with a desolvation system for sample introduction (Apex Q, ESI), allowed the determination of 29 major and trace elements (Li, Na, Mg, Al, Ti, V, Cr, Mn, Fe, Co, Ni, Cu, Zn, Ga, As, Rb, Sr, Nb, Mo, Ag, Cd, Sn, Sb, Cs, Ba, Tl, Pb, Bi, and U). All concentrations in the Guliya samples were several times higher than the instrumental detection limits determined by [55,67]. The measurements' accuracy and precision values were similar to those reported by [55,67]: measured concentrations of the TMRain-95 standard solution fall within the uncertainty limit of the certified concentrations and the precision is within 4–10% for all TEs except Nb and Sn (17%), and Ag (22%).

2.3.3. Enrichment Factor

The crustal enrichment factor (EF) is defined as the ratio of the concentration of a given trace element (TE) to that of an element (X) that is stable and abundant in rock and soil, typically Fe, Al, or Ti. This ratio $(TE/X)_{spl}$ is normalized to the same ratio obtained from a crustal reference $(TE/X)_{ref}$:

$$EF = (TE/X)_{spl}/(TE/X)_{ref} \tag{2}$$

The ice samples and dust filters selected for this preliminary study have been sampled from layers that are too old to have been contaminated by the deposition of anthropogenic emission products. Therefore, instead of highlighting the anthropogenic contribution to the sample's elemental budget, the EF is used here to extract subtle compositional differences among samples. The preparation (i.e., acid leaching) and analysis by ICPMS of the Guliya ice samples followed the same procedures as those employed by [55,68] to characterize the PSA soil samples collected from the vicinity of Guliya glacier. Consequently, this set of PSA soils is the preferred crustal reference used in the calculation of EF for the ice samples. However, for the digested dust filter samples, the Upper Continental Crust (UCC) composition [69] is the chosen crustal reference because UCC concentrations were determined by X-ray fluorescence spectrometry and atomic absorption spectroscopy [70,71], which provides total elemental concentrations comparable to those obtained after the full acid digestion of the dust filter samples.

3. Results and Discussion

3.1. Spatial and Temporal Variability of Dust Concentration, Size, and Mineralogy

3.1.1. Dust Concentration and Particle Size Distribution in Ice Samples

The dust concentration shown in Figure 3 corresponds to the median concentration of discrete samples or "subsamples" (n: number of discrete subsamples; Table 1) analyzed in each ice sample (i.e., each ~1 m ice section) of interest. Samples from GS display higher dust median concentrations than any of the GP ice samples investigated, except for T309 in the deep GP layers. This result is expected considering the lower annual snow accumulation at the Summit compared to the Plateau site. However, because the age of the GS samples is not yet determined precisely, their dust concentration cannot be readily compared to those of the GP samples. Generally, in GP, higher dust concentrations are observed in ice layers corresponding to cold periods when compared to warm periods occurring before and after them, which corroborates findings from the Guliya 1992 core [11,72]. This variability observed on an orbital timescale is comparable to that on a seasonal timescale for Guliya, where the highest dust storm frequency occurs during the coldest and driest season (i.e., late winter-early spring), when the Westerlies intensify [73,74]. An enhanced westerly circulation under a dry climate favors the transport of mineral particles over long distances, their size sorting while in route, and ultimately, their deposition onto high-altitude glaciers. This process likely contributed to the higher proportion of fine particles (<4 μm) observed in the GP samples for cold periods compared to those from warm periods (Figure 4a), even if both types of samples have a similar diameter size mode (8.4 μm (T225) and 8.6 μm (T233), respectively, Figure 4b). The more extensive snow cover around the Guliya ice cap during cold periods would inhibit the entrainment of dust from local sources, thereby further increasing the relative contribution of distant dust sources and finer dust.

Towards the bottom of GP, the ice is compressed, and 1 m of ice comprises more time, thereby smoothing out the changes in dust concentration between warm and cold periods (e.g., T262 to T278 during MIS5; Figure 3). For instance, this is characterized by the smaller 75th percentile of samples T273 (9×10^5 part. mL^{-1}) and T292 (8.7×10^5 part. mL^{-1}) compared to T308 (5.3×10^6 part. mL^{-1}). The largest variation in particle counts in the deepest part of the core coincides with the stratigraphic transition from mostly diffuse brown dust to mostly grey dust. The particle count is high when the grey aggregates (or nodules) occur in a sample taken from an ice section otherwise described as "clean" relative to the dustier upper layers of the core (Figure A1). The distribution of grey nodules is heterogeneous within the "clean" bottom ice layers. Therefore, the bottom GP ice samples can either contain grey nodules with numerous microparticles or are "clean ice" without nodules and yielding a low dust concentration. Towards the deepest part of GS, the volume size distribution of particles measured in T49 is bimodal with a primary mode in the fine grain silt-size at 10.6 µm (11.4% of dust volume), and a secondary mode in the clay-size range at 1.8 µm, which represents only 7.22 % of the dust volume in that sample (Figure 4b). The difference in particle size distribution between the bottom of GS (bimodal distribution) and the bottom of GP (predominantly clay-size fraction) is one of the most striking observations of spatial variability in the Guliya dust record.

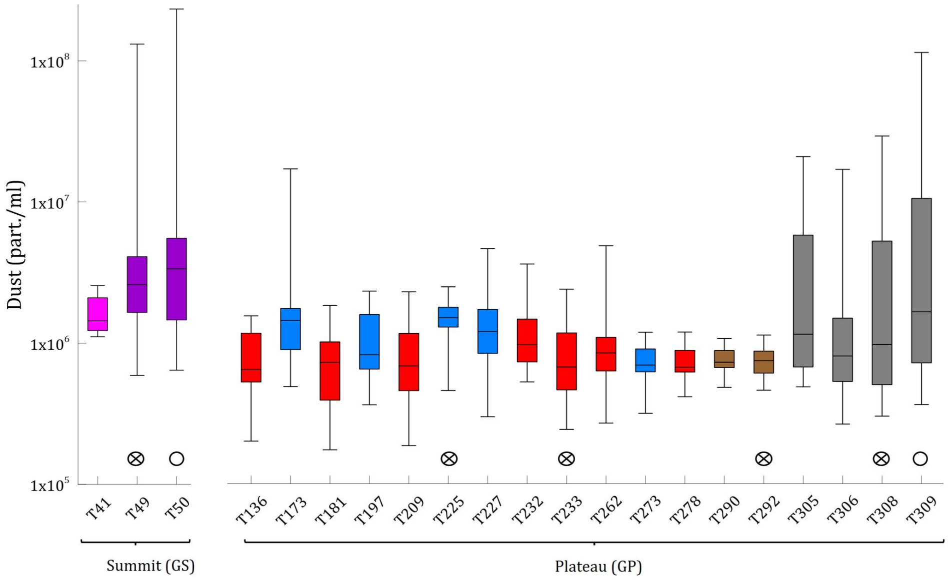

Figure 3. Dust concentration (number of particles/mL) measured by Coulter counter in 1 m ice sections from the GS and GP cores. For each section, the box represents concentrations falling within the 25–75 percentile range. The horizontal bar in the box is the median dust concentration, and the full data range is represented by the whiskers. The dust concentrations of ^{18}O-enriched or "warm period" ice samples are shown in purple (GS) and red (GP). The dust concentrations of ^{18}O-depleted or "cold period" ice samples are shown in pink (GS) and blue (GP). Dust concentration data for the deepest GP ice samples are shown in brown and grey, referring to the dust's dominant color, independent of the sample's mean $\delta^{18}O$ value. The circles mark in which 1 m section a dust filter was sampled and analyzed for elemental and isotopic geochemistry (crossed circles) or mineralogy (open circles).

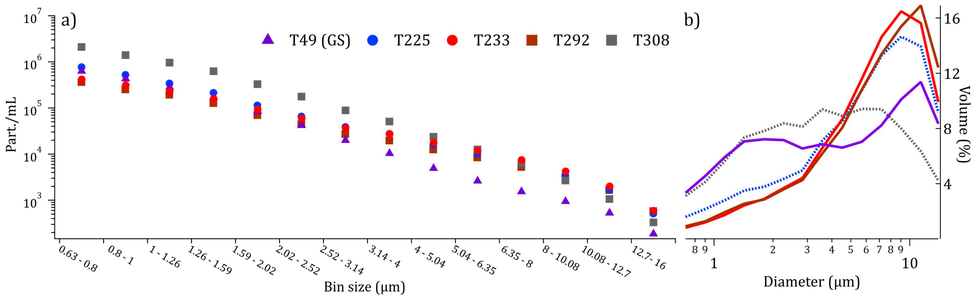

Figure 4. (**a**) number and (**b**) relative volumetric size distribution of microparticles measured by Coulter counter (14 bins) in 1 m ice sections prior to filtering.

3.1.2. Mineralogy of the Deep GS Dust Filter (T50): Dry Conditions and Proximal Influence

A wide range in grain sizes is observed on the T50 dust filter (Figure 5). Comparing the deepest layers of the two Guliya core sites, Figure 5 shows that the dust deposited on T50 (~48 m depth on GS) contains a higher proportion of silt and fine sand particles than on the plateau of the ice cap (i.e., T309 of GP). The subangular grain shape observed with SEM (Figure 5a), and the reduced size sorting suggest a more proximal source of aeolian sediments, or a mix of particles from proximal and remote sources. The angularity of the larger grains also supports a glacial origin. The occurrence in T50 of Ca-pyribole (pyroxene or amphibole), clinochlore (Mg-rich chlorite), subhedral calcite (Figures 5 and 6) and halite suggests relatively weak chemical weathering in the dust source region. This implies that the climate was particularly dry or that a stronger insolation would have favored the sublimation of the ice surface and crystallization of salts. Illitic clay dominates the clay-sized fraction of T50, whereas quartz, K-feldspar and biotite compose the bulk of the silt fraction, which is typical of a granitic mineralogy. The size distribution and its mineral composition make the dust in the deep layers of the GS core resemble that of the Taklimakan desert sands, which among central Asian deserts, contain the highest amount of calcite [36,75,76].

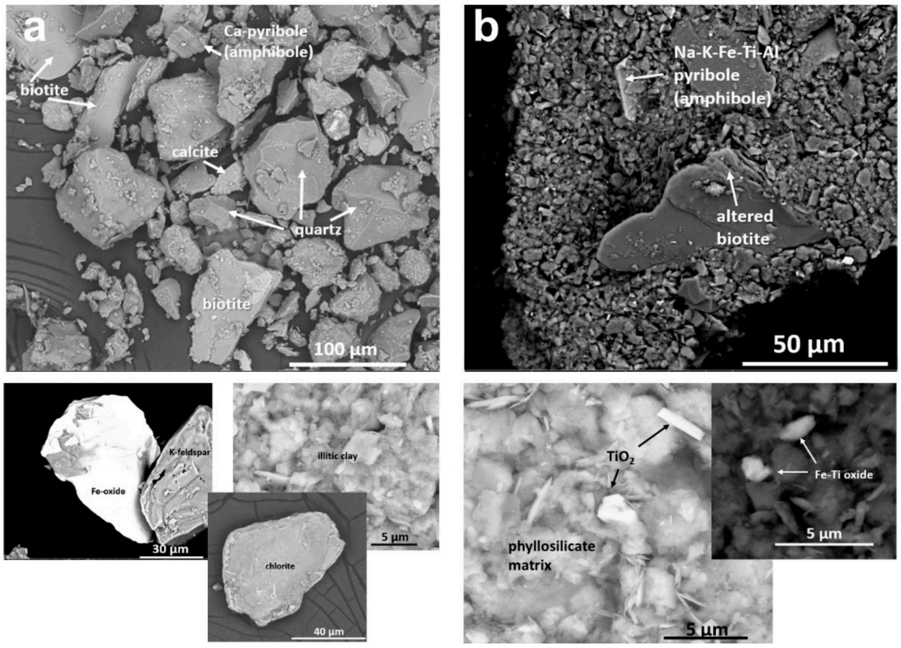

Figure 5. SEM (Scanning Electron Microscope) images of dust filters collected from (**a**) GS (T50) and (**b**) GP (T309).

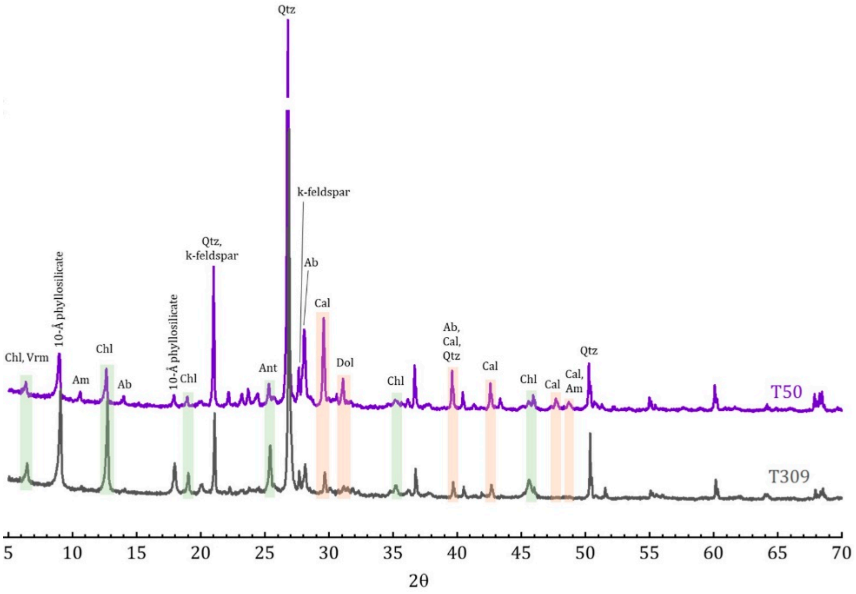

Figure 6. X-ray diffraction (XRD) patterns for the dust sampled from the deepest layers of the GS (T50) and the GP (T309) cores discussed in this study. The T50 diffractogram is shifted up to allow the identification of key features and to facilitate the visual comparison with T309. The orange and green shadings highlight minerals found in higher abundance, respectively, in T50 and in T309 (conventional mineral abbreviations from USGS.gov).

3.1.3. Mineralogy of the Deep GP Dust (T309): Grey Clay from a Weathered Source

The GP ice section T309 corresponds to a depth where small (1–5 mm) to large (<1.5 cm) scattered nodules of grey dust are the only type of dust visible to the unaided eye (Figure A1). Upon melting the ice samples, these nodules disintegrated into very fine particles, yielding the highest microparticle concentration (median concentration = $1.6 \times 10^6 \pm 2.10^7$ part. mL^{-1}, Figure 3) and the finest particle size distribution (diameter median = 5.9 µm; diameter mode = 3.8 µm) among ice samples analyzed by Coulter counter (Figure 4).

The SEM analysis performed on the T309 dust filter (Figure 5b) confirms that the grey dust is mostly composed of clay-sized grains (<2 µm), with fewer silt-sized particles (<50 µm) of K-feldspar and bio-pyribole (biotite, amphibole, or pyroxene). The small size fraction could indicate a more efficient mineral sorting during long-range atmospheric transport of the microparticles to the ice cap, suggesting that the grey clay originates from a distant location. However, within the ice, the grey clay is observed as nodules. In a relatively wet environment, clay aggregates could have been entrained and transported from proximal clay deposits surrounding the glacier. Alternatively, nodules could be post depositional features. In some sections, dust nodules are concomitant to diffuse horizontal dust layers, which could argue that the grey clay was deposited already in the nodular form, or that the diffuse layers result from the smearing of a nodule along a shear plane. The aggregation of clay particles with time and depth [60] is another possible process that could explain the presence of the clay nodules (Figure A1).

The X-ray scan of T309 (Figure 6) indicates that the grey clay is composed of illite, mica (biotite/muscovite), chlorite and vermiculite. SEM imagery (Figure 5b) shows that biotite is occasionally physically weathered (rounded folia). Compared to other filter samples, the grey and green color of the dust layers visible in the deep sections of the GP core could reflect the occurrence of more ferrous (Fe^{2+})-bearing minerals such as Fe-Ti oxides (Figure 5b) [77], or a larger amount of chlorite or other Fe-bearing phyllosilicates.

Heavy REE-bearing phosphates, such as xenotime and monazite, are also found in the silt and clay-sized fraction (1–2 µm) of the bulk T309 sample, identified by EDX microanalysis (Figure A3). Potentially REE-bearing coarse fluorapatite minerals (20 µm) found in T309 are a common accessory mineral in various rocks, nevertheless they could also possibly indicate the hydrothermal nature of the dust source. Clay to fine silt-sized needles of iron and titanium oxides (ilmenite, spinel, rutile or anatase), which are resistant to weathering, are detected in higher proportions than in other samples (Figures 5b and 6). Titanium oxides are derived from the weathering of igneous and metamorphic rocks and sediments. They can also form in soils from the weathering of less-resistant minerals (e.g., biotite, amphibole) [78]. The higher occurrence of small titanium oxide needles or equant-shaped grains in the deepest GP ice layers provides additional evidence that the source of aeolian particles to NW Tibet was subject to more substantial weathering prior to 110 kyr BP.

3.2. Elemental and Isotopic Composition of the Dust: Paleo-Environmental Implications

3.2.1. Trace Element Geochemistry

Dust filters. Elemental EFs for dust filter samples are shown in Figure 7. EFs do not covariate with the concentration of the crustal element of reference Ti in the filter samples (Table A1) and thus the influence of Ti on EF can be ruled out. The Sr EF in GS T49 (EF_{UCC} Sr = 0.74) is notably higher than those of the four GP filters analyzed (EF_{UCC}Sr = 0.22 (T225); 0.35 (T233); 0.27 (T292) and, 0.22 (T308), Table A1). This is consistent with the previously described mineralogical composition of the adjacent T50 dust filter, which includes calcite and halite. As strontium abundance in Chinese loess is controlled by carbonate [79], the higher Sr enrichment in T49 is likely associated with the larger amount of calcite in the dust, indicative of mixing with calcite-rich Taklimakan desert dust. The higher Sr EF in dust from "warm" intervals (T233) compared to that of dust filters from "cold" GP sections (T225) could also reflect a larger input of calcite-rich Taklimakan desert dust during warm periods.

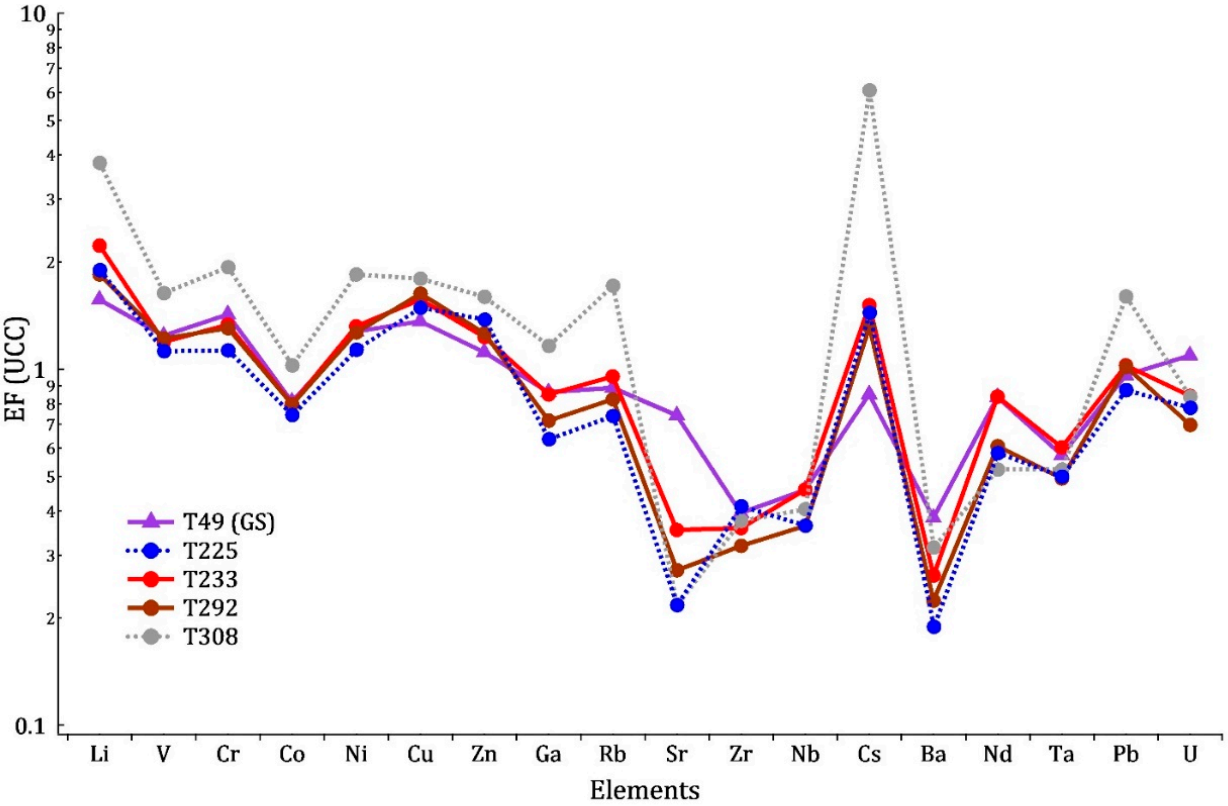

Figure 7. Enrichment factor (EF) of 18 TEs analyzed in GS and GP dust filters. EF is calculated using Ti as the TE of reference (Fe was not analyzed in the filters) and the Upper Continental Crust (UCC) [69] as the crustal reference.

For the two types of dust in GP, the elemental analysis of the brown (T292) and the grey (T308) dust filters shows that the former is enriched in Sr; while the latter is enriched in Li, Rb, Cs and Pb, similar to Southern Tibetan loess [80,81] and to Tibetan geyserite deposits [82]. The high abundance of Pb in the grey dust could suggest an affiliation of Pb to phosphate minerals, zircons or to K-feldspar, which is commonly found in NW China granites for instance [83]. Particle size measurements previously showed that the grey dust microparticles are much smaller (average particle diameter <2 µm) than those of the brown dust (Figures 4 and 5). The T308 enrichment in Cs (EF_{UCC} Cs = 6) relative to the other filters is consistent with the presence of grey clay at the bottom of the core because clay minerals, such as vermiculite, tend to adsorb and sequester Cs^+ and Rb^+ ions [80,84]. This adsorption mechanism by clay minerals and the release of ions in the melted ice sample, could also partially explain the higher F^- concentrations measured in Guliya ice samples (Figure A4 and [85] there in) with high content of grey clay particles compared to those with brown dust [86]. Studies of trace elements in granites show that Cs, Li, and F (among others) can be expelled at the end of crystallization of granitic magma to form pegmatites and released in geothermal waters and sediments ([87] and reference therein). For example, refs. [87,88] studied thermal springs and salt lakes in Tibet and found that many geothermal fields produce B, Li, and Cs-rich waters. Northern China is one of the regions of the world with the highest fluoride concentrations in its groundwater [85] (Figure A4). Thus, it is possible that the Cs, F, and Li-rich clay found in the deep part of the GP core originated from clay sediments of salt lakes or rivers fed by geothermal waters [89].

Ice samples. Elemental analyses performed on GS ice samples (Figure 8a) and the GP “warm” (Figure 8b) and “brown dust” (Figure 8c) ice samples confirm the relative enrichment in both Sr and soluble elements such as Na, Nb, Mo, Sn and U (Table A2). Considering the high solubility of Mo in oxic systems and under alkaline conditions in calcareous soils [90], its enrichment in “warm” (i.e., ^{18}O-enriched) and “brown dust” ice samples (EF_{PSA} Mo = 1.87 and 1.35, respectively) would indicate that Mo is desorbed from alkaline dust contained in the ice. The Mo desorption from the dust and its dissolution in solution may have occurred during the melting phase of the sample preparation (see Section 2.3.2.). Conversely, the noticeably lower Mo enrichment observed in "cold" (i.e.,^{18}O-depleted) (EF_{PSA} Mo = 1) and "grey dust" ice samples (EF_{PSA} Mo = 1.12) (Figure 8b) suggests that these two types of samples contain acidic dust in which Mo is adsorbed more efficiently on mineral surfaces (e.g., Fe-oxides) [91], and thus is less easily released into the liquid ice sample. While Mo enrichment could reflect alkaline conditions in the ice, confirmation of Mo enrichment as a reliable proxy for dry climate conditions (with weaker chemical weathering) requires the analysis of sufficient additional Guliya ice core samples to achieve a statistically significant result.

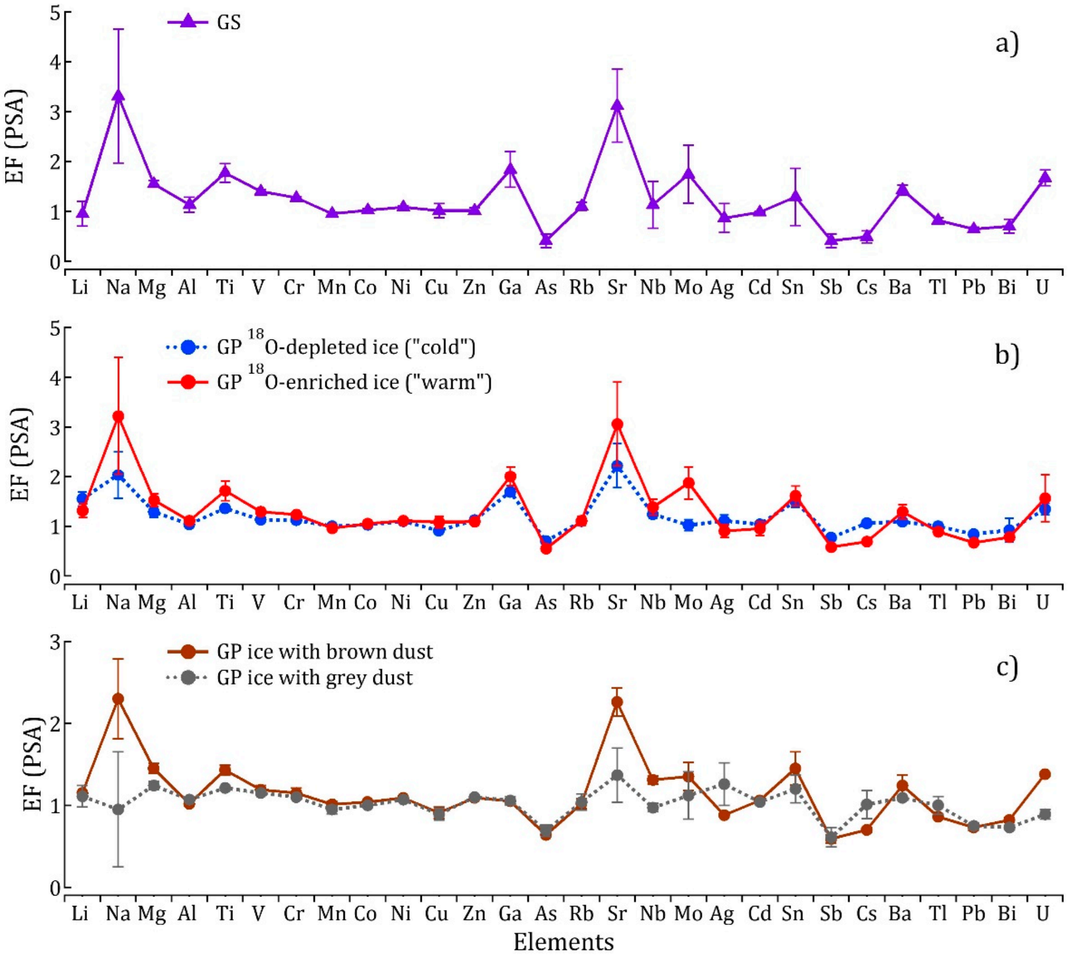

Figure 8. TE average (± st dev) enrichment factor (EF) in ice samples from (**a**) GS, (**b**) ^{18}O-depleted (cold) and ^{18}O-enriched (warm) GP sections, (**c**) GP ice sections containing "brown" or "grey" dust. EF is calculated using Fe and the local PSAs [55] as the crustal references. Here, Fe is the preferred crustal element of reference to illustrate the Ti enrichment variability among the various types of ice samples.

Enrichments in Ag and to a lesser extent Tl in the ice containing grey clay (Figure 8c) seem to be characteristic of Chinese aeolian soils, as they were previously observed by [55,68] in samples collected, respectively, across the TP and in the vicinity of the Guliya ice cap. The relatively higher enrichment in Cs of the ice sample with grey dust compared to the ice with brown dust confirms the results obtained for the filter analysis: the GP grey clay is composed of Cs-hosting minerals such as vermiculite (Figure 6) [84].

3.2.2. REE and Sr and Nd Isotopic Composition of Dust Filter Samples: Provenance Keys

The five dust filters were analyzed for REE and Sr-Nd isotopes (Table 1). Their signature for their chondrite normalized REE patterns and for two size-independent provenance tracers (i.e., δEu_N and $(La/Yb)_N$, [76]) are given, respectively, in Figures 9 and 10. Chondritic normalization has been chosen over shale (PAAS) normalization to create more spread-out patterns and more readable figures. The chondrite normalized REE distribution patterns are generally homogeneous (Figure 9 and [92,93] there in) with a negative Eu anomaly (δEu_N, Table A3), a steep light REE enrichment (LREE includes La to Eu), and a relatively flat heavy REE profile (HREE includes Gd to Lu) characteristic of Chinese loess [36,76,94,95]. The ratio of La_N to Yb_N is a measure of the overall enrichment in LREE (Figure 10).

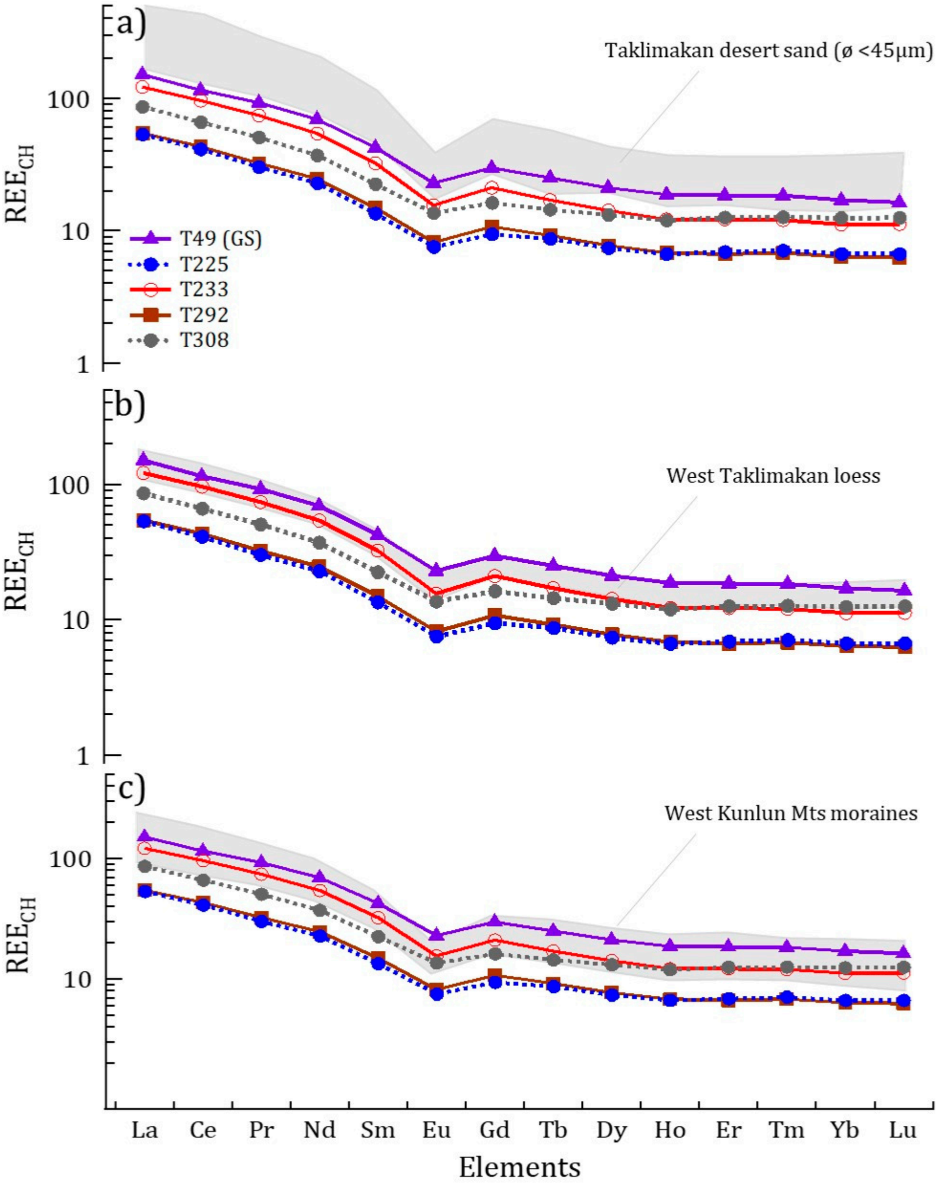

Figure 9. Chondrite-normalized REE patterns of dust filters from GS and GP ice cores compared to (**a**) Taklimakan fine desert sand, (**b**) West Taklimakan loess [36] and to (**c**) moraines of west Kunlun Mountains [92] represented by the shaded area. REE abundances in the C1 chondrite [93] are used for normalization.

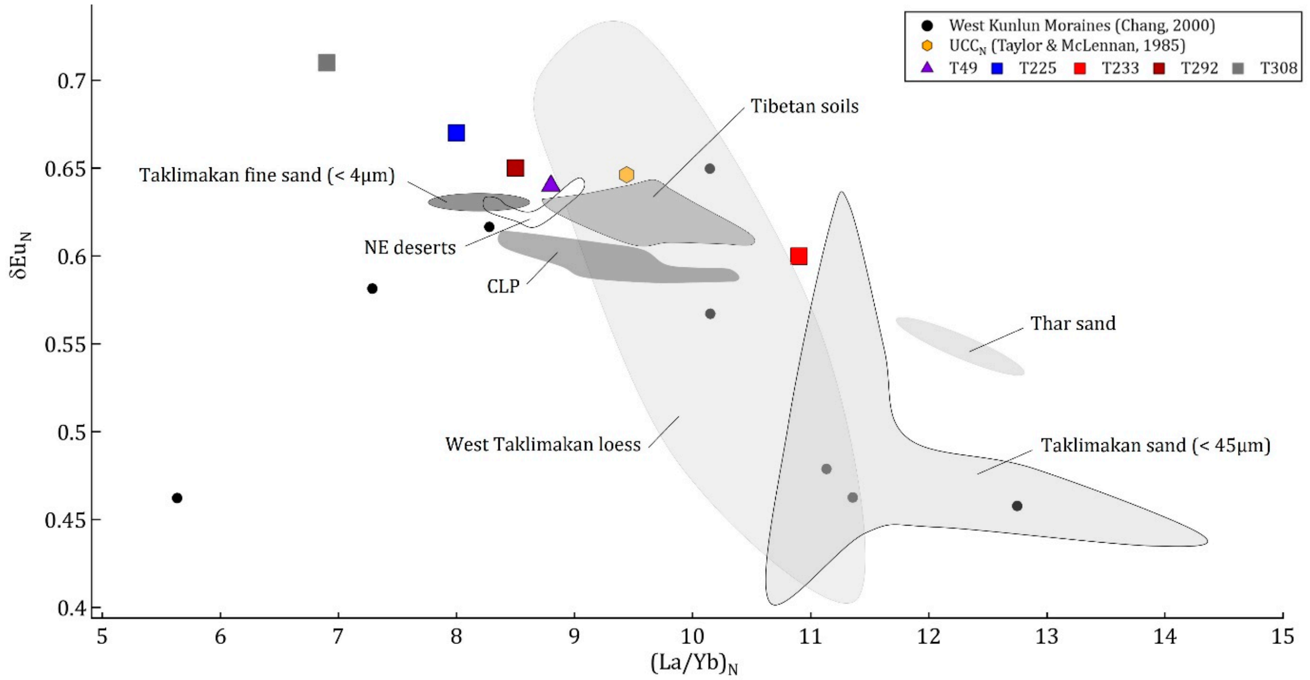

Figure 10. REE-based provenance signatures of Guliya dust filters compared to that of the Upper Continental Curst (UCC) [94] and the Central Asian deserts: Chinese Loess Plateau (CLP) loess; Taklimakan fine sand; Northeast deserts (Mu Us, Hobq, and Badain Jaran deserts); Tibetan soils, and Thar desert [76]; West Kunlun moraines [92]; and Taklimakan sand and West Taklimakan loess [36]. The N subscript in δEu_N and $(La/Yb)_N$ indicates that values are normalized to the C1 chondrite [93].

Among the five dust filter samples, T233 (“warm” GP) exhibits the highest $(La/Yb)_N$ ratio (10.87) and the lowest δEu_N (0.60), which implies that fewer HREE-carrier minerals (e.g., clays) and relatively more plagioclases compose the mineralogy of T233. δEu_N for T233 (Figure 10) falls within range of Eu anomalies measured in CLP [76] and West Taklimakan loess [36], while its REE pattern (Figure 9) matches that of West Taklimakan loess and West Kunlun Moraine [92]. This suggests that the T233 dust deposited during MIS 5a on the glacier plateau could be a mix of loess and moraine material originating west of the ice cap. However, caution is required when comparing the geochemistry of late Pleistocene Guliya dust samples with that of modern moraine sediments and surface loess deposits, as these are possibly much younger than the deeper layers of the Guliya ice cap. For instance, [80] reports the lack of loess deposits older than 13 kyr in southern Tibet due to their erosion and recycling during glacial-interglacial cycles of the Quaternary. Thick (up to 700 m) and old (~800 kyr) loess deposits border the northern flanks of the western Kunlun Mountains [96], but to our knowledge, no Sr-Nd isotopic data have been reported for the Late Pleistocene layers of these sequences. This supports the strong relevance of the oldest Guliya glacial dust as an invaluable aeolian archive in the region. The Summit dust (T49) displays the second highest enrichment in LREE with a $(La/Yb)_N$ ratio of 8.83 compared to 8.54 for T292, 8 for T225 and 6.93 for T308. Because LREEs are less stable during weathering [14,97], their slightly higher enrichment in T49 is consistent with the presence of soluble and weathering-sensitive minerals (e.g., calcite; see Section 3.1.2) found in T50. The limited chemical weathering that affected T49 dust indicates dry climatic conditions prevailing at the source and in the Guliya region at the time of its deposition onto the ice cap surface. Figure 9 provides additional information on the possible dust source. The HREE part of the T49 REE profile falls within range of that of the Taklimakan desert sand and the West Kunlun moraines (Figure 9a), while the LREE part and its moderate Eu anomaly ($\delta Eu_N = 0.64$) are more typical of the West Taklimakan loess (Figure 9b). Dust filter T308 (“grey dust” from GP) exhibits the least negative Eu anomaly ($\delta Eu_N = 0.71$), which could result from the combined influence of vermiculite possessing a positive Eu anomaly [14], and of the smaller amount of plagioclase detected in the grey clay (Figure 6). Eu-hosting plagioclase minerals are characterized by a negative Eu anomaly as they release Eu^{2+} during weathering [98]. Therefore, less plagioclase could weaken the negative Eu anomaly of the grey clay. The reduced L/HREE fractionation in T308 is also the smallest reported here (L/HREE = 2.61 and $(La/Yb)_N = 6.93$, Table A3) and is linked to the relatively high abundance of weathering resistant phases such as Ti-oxides, zircons or phosphates in which HREE are preferentially present (Figure A3) [14,99]. The REE abundances in T292 ("brown dust" GP) and in T225 ("cold" GP) are lower than those of T49, T233 and T308 (Figure 9). Their REE patterns are quasi-identical and their Eu anomalies ($\delta Eu_N = 0.67$ and 0.65, respectively) are typical of the average upper continental crust [94] and of fairly well mixed sediments.

To track the geographical source of strontium and neodymium, $^{87}Sr/^{86}Sr$ and ε_{Nd} results for the bulk Guliya dust are matched to values reported in the literature for silt-sized surface dust samplesthe last glacial period as reported by [37]. However, until more evidence is gathered, the CLP situated due east of the Kunlun Mountains is not considered a potential source of aeolian dust to Guliya ice cap because wind patterns are assumed to be more westerly such that part of the CLP material originates from the NW Chinese deserts and the Kunlun moraines [36,92]. Furthermore, drawing conclusions regarding the differential influence on the Summit versus the Plateau sites would require sampling the dust material in ice layers of the same age in both cores, which was not feasible for this study as the GS time scale was under development. When compared with data from other Chinese glaciers (Figure A5) and glaciers around the world (Figure A6, and [100] there in), the Sr-Nd isotopic composition of the T49 GS dust filter resembles that of modern dust collected from Tien Shan glaciers, which was found to originate from the northern boundary of the Taklimakan desert and, to a lesser extent, from the Gurbantünggüt desert [48]. The Sr-Nd isotopic values for the GP samples (except for T308) are homogeneous and indicate that either (1) the mineral dust deposited on the Guliya Plateau was well-mixed in the atmosphere, or (2) the time encompassed by 1 m of ice in the deep layers of the Guliya glacier is so compressed that dust from multiple sources are contained in a single sample (filter). The potential multiple sources of GP dust could then be similar to those of the dust collected from the Miaoergou shallow core (Eastern Tien Shan), with isotope values overlapping those of Guliya (Figures A5 and A6) and that were interpreted as a mixture of Taklimakan and, Gobi deserts material [43]. It is then possible that the GP dust also originates from these two sources even though it does not plot along mixing lines (not shown) between the fields defined by Taklimakan sand and loess and the Gobi Desert.

The GP samples differ from the Dunde ice cap's modern dust samples [35]. ε_{Nd} for T225 (-9.55 ± 0.23) is the closest value to the Dunde signature, suggesting that, under cold climate conditions, some northern desert material from the Tarim and/or Qaidam Basins could also be entrained on the surface of Guliya. The $^{87}Sr/^{86}Sr$ of the grey dust (T308) is unusually high ($^{87}Sr/^{86}Sr = 0.72425$, Table 2) and unmatched among Chinese glacier dust signatures reported to date. This reveals the uniqueness of the material preserved in the bottom of the Guliya Plateau core which could reflect its old age and the unknown environmental setting at that time in northwestern Tibet. As the Sr isotope ratio is easily altered by grain size sorting [101,102], it is also possible that the higher $^{87}Sr/^{86}Sr$ value partly reflects the finer grain size fraction composing the material in T308. The origin of this grey clay could be determined by matching its Sr-Nd signature to that of the finest fraction (< 5 μm) of potential source area samples (Figure 11) as T308 dust is naturally size-sorted to the clay fraction (Figure 4). Its signature falls into the same range as those of the clay-sized CLP loess deposited between 20 and 50 kyr BP [30] and of a surface sample from the Qaidam desert [37], which likely indicate a common origin. However, other sources for T308 cannot be excluded until the analysis of the Guliya dust is rigorously constrained to its silicate fraction and its clay-size fraction. We intend to apply those constraints to future isotopic analyzes of Guliya dust samples.

Table 2. Sr-Nd isotopic composition of dust filter samples.

Sample ID	Size (µm)	Sr (ppm)	$^{87}Sr/^{86}Sr$	Error (2 σ)	Nd (ppm)	$^{143}Nd/^{144}Nd$	Error (2 σ)	ε_{Nd}
T49	>0.2	339.75	0.71457	0.00003	31.33	0.51217	0.00001	−9.14
T233	>0.2	126.1	0.71775	0.00002	24.48	0.51216	0.00001	−9.33
T225	>0.2	47.05	0.71832	0.00002	10.3	0.51215	0.00001	−9.55
T292	>0.2	61.01	0.71820	0.00003	11.15	0.51217	0.00001	−9.04
T308	>0.2	84.94	0.72425	0.00003	16.76	0.51215	0.00002	−9.58

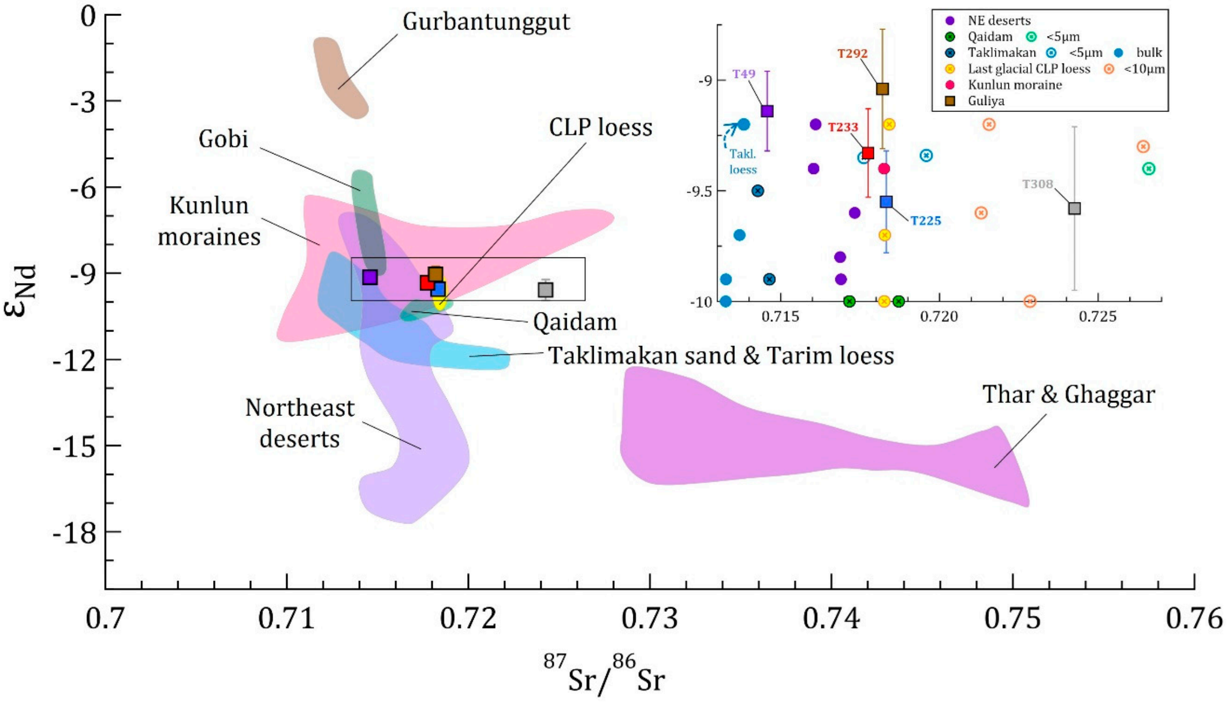

Figure 11. ε_{Nd} vs. $^{87}Sr/^{86}Sr$ of the five Guliya dust filters (squares) compared to Sr and Nd isotopic arrays of (<75 µm) dust sampled in Chinese deserts: Gurbantunggut, Qaidam [37], Gobi [26], Taklimakan sand and Tarim loess [36,37], Kunlun moraines [92], CLP loess [37], Northeast deserts including Mu Us, Hobq and Badain Jaran deserts [36]; and Indian deserts Thar [39] and Ghaggar river sediments [103]. The inset identifies the dust filter samples (squares) shown in the main figure and individual data points for the Chinese deserts' arrays within the rectangle. Data points for the clay-size fraction of surface Qaidam sand (<5 µm, [37]) and last glacial CLP loess (<10 µm, [30]) are also shown (crossed circles) as they can be compared to the naturally size sorted T308 sample (fine grey clay).

3.3. GP Grey Clays: A Possible Biological Influence

The grey color of the clay trapped within the deepest layers of the GP ice core (T309) is associated with the presence of phyllosilicates (chlorite, biotite, vermiculite) and oxides containing reduced iron (Fe^{2+}), while the reddish-brown colors of the shallower diffuse dust layers are characteristic of sediments containing ferric (oxidized) iron (Fe^{3+}) [77]. In pedology, a grey color is generally used as an indicator of anaerobic (oxygen-free) conditions, which occurs when soils are water-saturated (e.g., wetland) and anaerobic bacteria are present [104]. During respiration, these microorganisms utilize as nutrients the oxidized forms of elements such as N, Fe, Mn, and S, which become chemically reduced. Therefore, nitrate (NO_3^-), manganese (Mn^{4+}), iron (Fe^{3+}) and sulfate (SO_4^{2-}) are depleted by anaerobic respiration and, respectively, converted to NH_4^+, Mn^{2+}, Fe^{2+}, and HS^-. These additional indications that the grey dust originates from water-saturated soils or wetland soils could support our hypothesis of a wetter or a warmer climate at the time the deepest Guliya ice layers were deposited. Nonetheless, the post-depositional microbial activity could also account for the reduction of Fe in clay minerals within the ice. The fact that the grey clay nodules and the diffuse layers of brown dust are occasionally found within the same ice horizon (Figure A1), suggests that anaerobic bacteria are present on the grey clay particles only. A thorough microbiological analysis, like that performed by [105], combined with further mineral analyses of the oldest layers of the GP core would be instrumental in determining whether iron in the nodular grey clay has been reduced in situ by anaerobic microorganisms. No melt features (e.g., clear, non-bubbly ice) were observed around the clay nodules, which precludes the possible cryoconite nature of the nodules.

4. Conclusions

This preliminary physical, mineralogical, and geochemical characterization of dust particles from deep layers of the Guliya ice cap provides a rare glimpse of the aeolian dust composition that predates the Last Glacial Maximum. The comparison between the deep layers of the Summit and the Plateau sites and between stadial and interstadial transition layers of the Plateau core reveals the high variability of the Guliya dust record and demonstrates its value as an indicator of paleo-environmental conditions prevailing in NW Tibet since the Late Pleistocene.

The reduced size sorting and the angular shape of coarse grains on dust filters from the deep layers of the GS core indicate a mix of proximally and distally sourced aeolian material. The silt fraction is dominant, and its granite-like mineralogy also includes Ca-pyribole (amphibole), chlorite (clinochlore), and100 calcite and halite. This composition is consistent with the enrichment in soluble Sr and Na of the ice samples containing these dust layers and is indicative of weak chemical weathering and dry climatological conditions at the time the dust was entrained, transported, and deposited onto the ice cap. The higher $(La/Yb)_N$ also reflects the moderate weathering experienced by the deeper (older) Summit dust. The Summit dust REE pattern and ε_{Nd} vs. $^{87}Sr/^{86}Sr$ signature indicate that its source is likely in the Taklimakan desert, even though only a size-resolved isotopic analysis could allow the differentiation of distal and proximal provenances.

The investigation of samples from ice sections preceding and succeeding stadial/interstadial (cold/warm) transitions shows that the dust from "warm" GP ice shares some of the characteristics of the GS dust. In particular, its enrichment in Sr and in other soluble TEs (i.e., Na, Nb, Mo, Sn, and U) and its more fractionated L/HREE are indications that weathering-sensitive minerals have been sourced and transported to the glacier surface under a drier climate. However, contrary to the GS dust, the REE pattern and the ε_{Nd} vs. $^{87}Sr/^{86}Sr$ signature of the "warm" GP dust do not point to a distinct geographical source but rather to a mix of West Taklimakan loess and West Kunlun moraine material. This preliminary study of the dust from warm/cold transitions also reflects the larger contribution of clay-size particles to the total dust volume during cold periods. This, and the upper continental crust-like REE pattern of the dust from a "cold" GP section, suggests that the ice cap then receives a bigger proportion of well-mixed, long-range-transported dust. This mix could possibly originate from the north and the Tarim and Qaidam Basins as suggested by its isotopic signature, similar to that of the modern dust from Dunde ice cap.

This work also describes the dust from the GP ice core layers older than 110 kyr, which is present in various unusual stratigraphical forms: diffuse horizontal brown or greenish layers, discrete scattered particles, and grey nodules. The geographical source of the grey dust nodules cannot yet be confidently ascertained as its more radiogenic $^{87}Sr/^{86}Sr$ value could only be approximately matched to the fine CLP loess deposit and fine Qaidam surface sands. However, its preliminary geochemical characterization already provides important paleo-environmental information and keys for further interpretation of the GP ice core archives. The grey dust is well size-sorted and composed mainly of phyllosilicates (illitic clay, biotite, chlorite, vermiculite), Ti-oxides (anatase, rutile, or brookite), K-feldspar, and trace xenotime and monazite, which are resistant to weathering. The abundance of

Fe/Ti-oxides and the inherent enrichment in HREE are additional evidence that the bottom mineral dust experienced intense chemical weathering, suggesting wet conditions at the source. At this depth in the core, the ice enrichment in Rb, as well as in Cs, Li, and F may be explained by the presence of vermiculite and its high adsorption capacity of these elements in their ionic form. It is therefore suggested that geothermal waters, highly concentrated in Cs, F, and Li, may have contributed to the leaching of the grey dust before its deposition on the Guliya Plateau more than 110 kyr ago.

These initial results are encouraging and demonstrate the importance of characterizing additional samples from these two cores to develop higher resolution Guliya dust records. Investigating the temporal variations of isotopic and elemental geotracers in the Guliya ice will afford the opportunity to gain new insight into regional paleo-synoptic conditions, including their variability and associated environmental changes. Future research on compositional changes in the dust will also provide a fundamental reference for biological investigation of microbial populations within the ice and their evolution over different time periods.

Author Contributions: L.G.T. and E.M.-T.: Conceptualization, funding acquisition, project administration, supervision. E.B., J.M.S., E.M., M.R.S.-H.: methodology, formal analysis, investigation, validation. E.B.: visualization, writing- original draft. All the authors: Writing—Review editing. All authors have read and agreed to the published version of the manuscript.

Funding: Financial support was provided by the National Science Foundation (NSF) P2C2 program awards 1502919 and 2002521.

Data Availability Statement: Datasets related to this article can be found at: https://www.ncei.noaa.gov/products/paleoclimatology/ice-core (accessed on 28 September 2022), hosted at NOAA's National Centers for Environmental Information for Paleoclimatology.

Acknowledgments: We thank Donald Kenny (BPCRC) for the size and concentration measurements of microparticles and for the collection of dust filters. We thank Ping-Nan Lin (BPCRC) for the oxygen isotopes measurements. We acknowledge the technical assistance of Daniel Fischer and George Kamenov (University of Florida) and Paolo Gabrielli (BPCRC) with the geochemical analyses on the MC-ICP-MS and the ICPMS, respectively. This is Byrd Polar and Climate Research Center contribution number C1620.

Conflicts of Interest: The authors declare no conflict of interest.

Appendix A

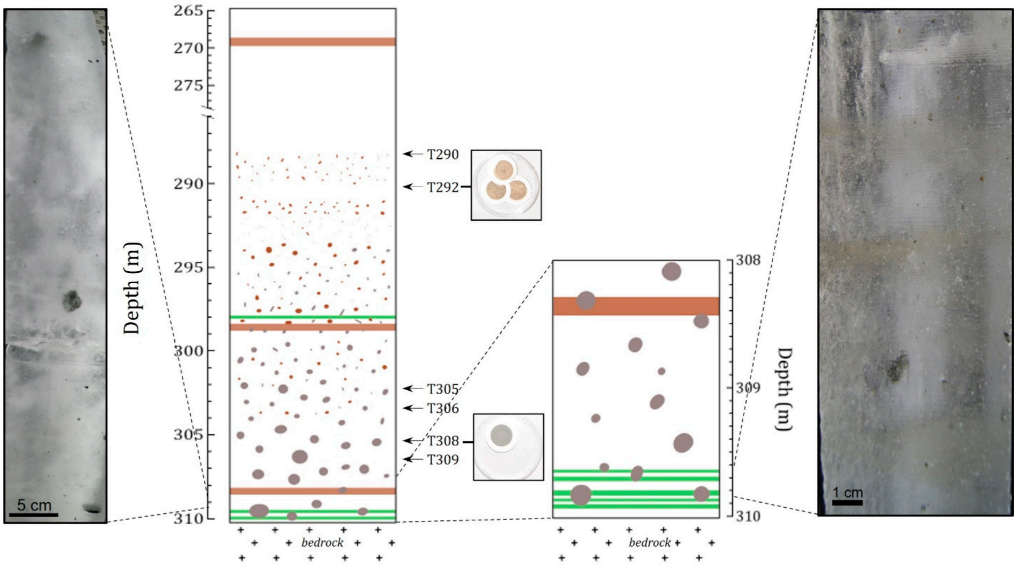

Figure A1. Simplified visual stratigraphy of the deepest 45 m of the GP ice core. Horizontal bars in the sketch mark the location of diffuse brown or greenish dust layers. Dots of various sizes symbolize dust particles and nodules. The grey dust nodules are larger within the deepest 5 m of the core. Note that the size of particles and nodules is not at scale in the sketch. The arrows point to the top depth of the 6 deepest 1 m ice sections discussed in this paper. The color difference is still noticeable among dust filters, as shown here in small photos of T292 and T308 filters. Photos of deep ice core sections show the grey nodules (T311, **left**) and horizontal diffuse layers (T312, **right**). Bubbles are present throughout the core and extend all the way to the bedrock, confirming the ice's meteoritic nature. The nodules' increasing size with depth could reflect growth by aggregation with time [60]. Smaller and much less conspicuous grey nodules have been observed in shallower parts of the GP core, which are not discussed in this paper.

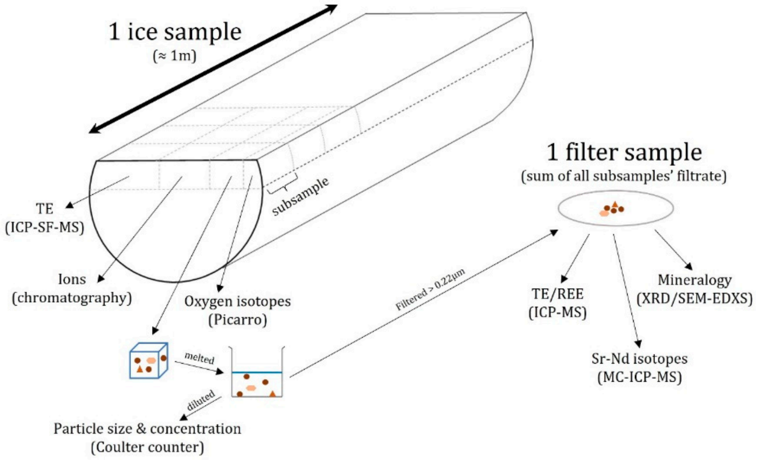

Figure A2. Sampling scheme of the ice and filter samples from a 1 m long ice core section of GP or GS. An ice sample is the entire 1 m section comprising subsamples which have been individually analyzed for trace elements (TE), major ions, dust size and concentration and oxygen isotopes. These parameters are not discussed at the subsample resolution in this manuscript. A filter sample corresponds to the insoluble particles (ø > 0.22 µm) collected by filtering all melted subsamples together on one filter.

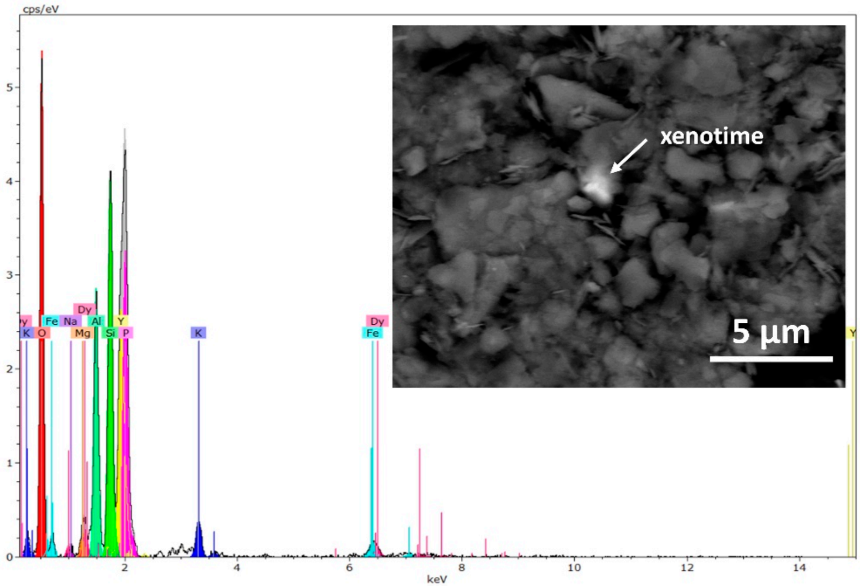

Figure A3. Spectral plot and Backscattered Electron (BSE) image of a HREE-bearing xenotime identified on dust filter T309 by EDXS trace mineralogy analysis.

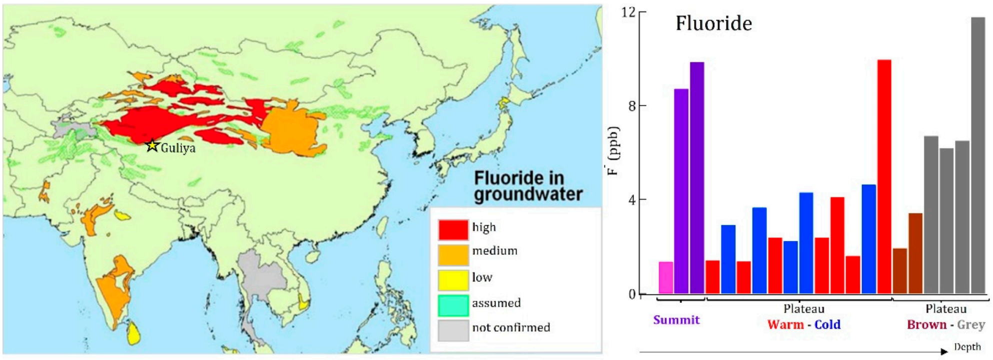

Figure A4. Probability of occurrence of excessive fluoride concentrations in Asian groundwater (left panel) [85] and median fluoride concentration (ppb) measured in 1 m ice samples from the Guliya ice cores discussed in this paper (right panel).

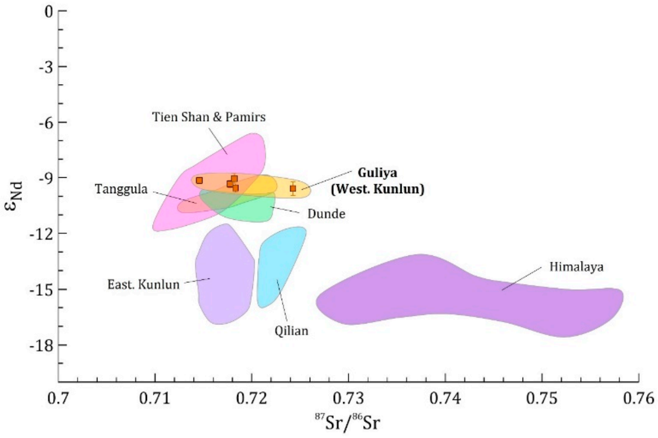

Figure A5. ε_{Nd} vs. $^{87}Sr/^{86}Sr$ of the five Guliya dust filters (brown squares) compared to Sr and Nd isotopic arrays of dust sampled in surface snow and shallow ice cores from Tien Shan and Pamirs [43,48], Tanggula, East Kunlun, Qilian [48], Dunde [35], and Everest (Himalaya) [44].

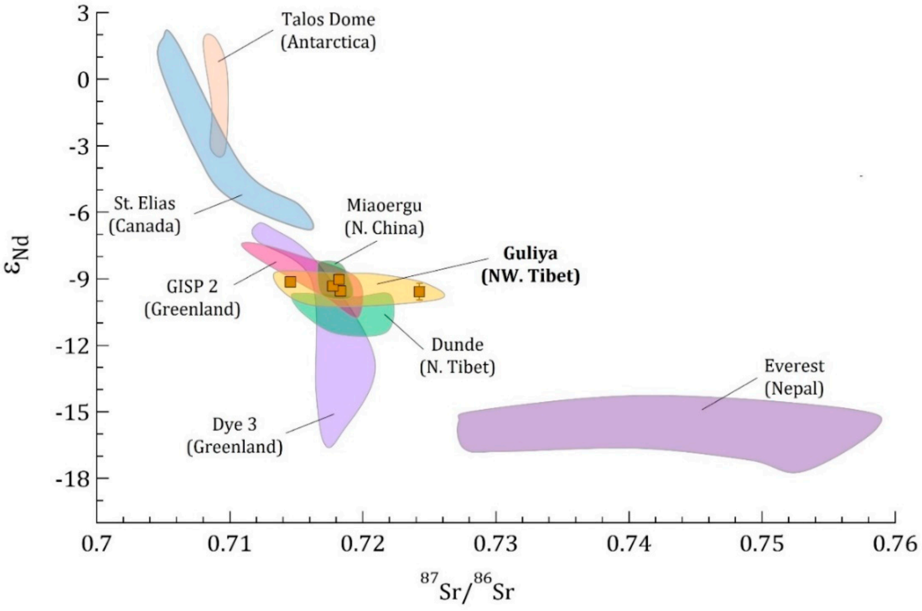

Figure A6. ε_{Nd} vs. $^{87}Sr/^{86}Sr$ of the five Guliya dust filters (brown squares) compared to Sr and Nd isotopic arrays of dust sampled in ice cores from: Dunde (China [35]), Miaoergou (China [43]), Everest (Nepal [44]), Mt. St. Elias (Canada [34]), GISP2 (Greenland [26]), Dye 3 (Greenland [22]) and Talos Dome (Antarctica [100]). These ice cores cover different time scales.

Table A1. TE enrichment factor of dust filters relative to the UCC [69]. Ti is the crustal element of reference and its concentration (ppm) in each sample is displayed in italics.

TE	T49	T233	T225	T292	T308
Li	1.57	2.22	1.90	1.85	3.80
Ti	1.00	1.00	1.00	100	1.00
V	1.24	1.19	1.12	1.22	1.64
Cr	1.43	1.33	1.13	1.30	1.93
Co	0.81	0.80	0.74	0.80	102
Ni	1.28	1.32	1.13	1.27	1.84
Cu	1.36	1.57	1.49	1.63	1.80
Zn	1.12	1.23	1.38	1.26	1.60
Ga	0.86	0.85	0.64	0.72	1.16
Rb	0.89	0.95	0.74	0.82	1.72
Sr	0.74	0.35	0.22	0.27	0.22
Zr	0.39	0.36	0.41	0.32	0.37
Nb	0.46	0.46	0.36	0.36	0.40
Cs	0.85	1.51	1.44	1.31	6.07
Ba	0.38	0.26	0.19	0.22	0.32
Nd	0.83	0.84	0.58	0.61	0.52
Ta	0.57	0.60	0.50	0.49	0.52
Pb	0.96	1.02	0.87	101	1.60
U	1.09	0.84	0.78	0.70	0.84
Ti (ppm)	*4518*	*2133*	*3516*	*2209*	*3863*

Table A2. Average TE enrichment factor in ice samples relative to local PSAs [55]. Fe is the crustal TE of reference.

	PSA	**Summit (GS)**		**Plateau (GP)**													
				Warm	**Cold**	**Warm**	**Cold**	**Warm**	**Cold**	**Warm**	**Warm**	**Cold**	**Warm**	**Brown**	**Brown**	**Grey**	**Grey**
TE	TE/Fe (ppt)	T41 (n = 11)	T50 (n = 10)	T136 (n = 9)	T173 (n = 9)	T181 (n = 7)	T197 (n = 5)	T209 (n = 7)	T227 (n = 8)	T232 (n = 9)	T262 (n = 9)	T273 (n = 9)	T278 (n = 10)	T290 (n = 16)	T292 (n = 16)	T305 (n = 17)	T306 (n = 16)
Li	1.8×10^{-3}	1.13	0.78	1.23	1.39	1.42	1.67	1.54	1.68	1.19	1.26	1.48	1.19	1.14	1.15	1.21	102
Na	2.7×10^{-1}	4.26	2.37	2.89	1.37	3.45	2.47	5.31	2.06	2.11	3.43	2.23	2.14	1.95	2.64	1.44	0.46
Mg	5.7×10^{-1}	1.60	1.50	1.55	1.22	1.43	1.38	1.77	1.18	1.45	1.45	1.39	1.48	1.41	1.49	1.28	1.20
Al	6.8×10^{-1}	1.23	1.03	1.10	1.14	1.22	0.99	1.13	0.99	1.12	102	1.05	1.06	101	1.04	1.08	1.06
Ti	3.1×10^{-2}	1.90	163	1.65	1.32	1.69	1.35	2.10	1.30	163	1.60	1.45	1.58	1.38	1.47	1.23	1.19
V	1.2×10^{-3}	1.43	1.37	1.25	1.21	1.40	1.09	1.38	1.07	1.27	1.23	1.17	1.22	1.16	1.23	1.17	1.13
Cr	1.0×10^{-3}	1.29	1.25	1.20	1.16	1.33	1.10	1.30	107	1.22	1.18	1.15	1.18	1.11	1.19	1.12	1.09
Mn	3.5×10^{-2}	0.97	0.92	0.97	0.99	0.99	1.03	1.00	1.00	0.89	0.95	0.97	0.96	103	0.98	0.99	0.92
Fe	1.0×10^{0}	1.00	1.00	100	1.00	1.00	1.00	1.00	100	1.00	100	1.00	1.00	1.00	1.00	1.00	100
Co	5.0×10^{-4}	1.04	0.99	103	1.04	1.08	1.08	1.14	1.01	1.01	1.04	1.01	1.02	104	1.04	0.99	1.01
Ni	1.2×10^{-3}	1.11	1.06	1.08	1.12	1.12	1.10	1.18	1.06	1.07	1.12	1.11	1.11	1.08	1.11	1.08	1.05
Cu	1.4×10^{-3}	1.12	0.91	1.05	0.90	1.12	0.94	1.09	0.83	0.96	1.29	0.95	0.98	0.86	0.97	0.94	0.85
Zn	2.8×10^{-3}	1.05	0.97	106	1.11	1.13	1.16	1.10	1.08	1.05	1.08	1.14	1.10	1.08	1.09	1.11	1.10
Ga	2.3×10^{-4}	2.09	1.59	1.98	1.79	2.11	1.60	2.30	1.65	1.95	1.91	1.70	1.76	104	1.07	103	1.10
As	1.2×10^{-3}	0.51	0.32	0.49	0.67	0.57	0.63	0.62	0.80	0.45	0.62	0.69	0.54	0.65	0.64	0.73	0.64
Rb	2.0×10^{-3}	1.15	1.04	1.01	1.17	1.14	1.01	1.27	1.12	1.06	1.10	1.08	1.06	0.98	1.06	1.11	0.97
Sr	8.2×10^{-3}	3.63	2.61	3.10	1.65	2.74	2.60	4.61	2.07	2.29	3.17	2.56	2.45	2.15	238	1.61	1.14
Nb	7.4×10^{-5}	1.47	0.80	1.13	1.21	1.42	1.12	1.58	1.31	1.34	1.31	1.31	1.47	1.28	1.35	101	0.94
Mo	2.4×10^{-5}	2.15	1.33	1.93	0.85	1.96	1.09	2.43	103	1.52	1.83	1.10	1.55	1.23	1.47	1.33	0.91
Ag	3.7×10^{-6}	107	0.66	0.86	1.09	0.95	1.09	1.13	1.27	0.74	0.89	0.97	0.87	0.89	0.88	1.44	1.07
Cd	9.8×10^{-6}	0.99	0.97	0.93	1.09	1.07	1.09	1.09	0.98	0.72	1.05	1.00	0.86	1.06	1.06	1.03	1.06
Sn	2.1×10^{-5}	1.69	0.88	1.33	1.36	1.86	1.55	1.63	163	1.46	1.79	1.45	1.58	1.30	1.59	1.33	1.08
Sb	$7.0\times 10^{-}5$	0.50	0.31	0.58	0.84	0.54	0.76	0.65	0.81	0.52	0.63	0.68	0.57	0.56	0.63	0.70	0.53
Cs	6.4×10^{-4}	0.57	0.41	0.66	1.13	0.63	1.01	0.76	1.11	0.65	0.73	0.99	0.73	0.72	0.69	1.13	0.89
Ba	6.4×10^{-3}	1.36	1.50	1.23	1.12	1.32	1.06	1.52	1.08	1.18	1.35	1.10	1.12	1.15	1.33	1.11	107
Tl	1.9×10^{-5}	0.86	0.78	0.86	1.12	0.90	0.97	0.99	0.98	0.83	0.92	0.94	0.86	0.85	0.87	1.08	0.92

Table A2. *Cont.*

	PSA	Summit (GS)		Plateau (GP)													
				Warm	**Cold**	**Warm**	**Cold**	**Warm**	**Cold**	**Warm**	**Warm**	**Cold**	**Warm**	**Brown**	**Brown**	**Grey**	**Grey**
Pb	1.2×10^{-3}	0.67	0.61	0.72	0.86	0.70	0.82	0.70	0.84	0.60	0.67	0.83	0.64	0.76	0.71	0.78	0.72
Bi	1.9×10^{-5}	0.80	0.60	0.80	0.79	0.80	0.84	0.78	1.29	0.77	0.81	0.79	0.70	0.84	0.80	0.75	0.71
U	6.1×10^{-5}	1.78	1.56	167	1.16	1.35	1.40	2.46	1.36	1.27	1.41	1.43	1.21	1.37	1.40	0.93	0.84

Table A3. REE and Sc, Y, Hf. and Th abundance in dust filters. Concentrations (ppm) are normalized to the C1 chondrite [93]. Normalized values (indicated by the N subscript) were also used in Eu anomaly ($\delta Eu_N = Eu_N/(Sm_N * Gd_N)^{1/2}$ and $(La/Yb)_N$ calculation.

Sample ID	La	Ce	Pr	Nd	Sm	Eu	Gd	Tb	Dy	Ho	Er	Tm	Yb	Lu	Sc	Y	Hf	Th	L/HREE	δEu_N	$(La/Yb)_N$
T49	150.7	115.0	92.4	69.3	42.5	22.9	29.7	25.0	21.1	18.7	18.5	18.4	17.1	16.4	2.4	20.4	35.1	449.5	2.99	0.64	8.83
T225	53.3	41.0	30.1	22.8	13.4	7.5	9.4	8.7	7.4	6.6	6.9	7.1	6.7	6.7	0.8	7.1	17.8	156.8	2.83	0.67	8.00
T233	121.4	96.1	74.0	54.1	32.3	15.6	21.0	17.1	14.2	12.2	12.2	12.0	11.2	11.2	1.6	13.1	25.7	361.3	3.54	0.60	10.87
T292	54.4	43.1	323	24.7	14.9	8.2	10.7	9.2	7.7	6.8	6.7	6.8	6.4	6.3	1.0	7.1	14.3	174.7	2.93	0.65	8.54
T308	86.1	65.9	50.5	37.0	22.5	13.6	16.2	14.4	13.1	11.9	12.5	12.6	12.4	12.5	2.3	12.9	29.3	347.4	2.61	0.71	6.93

References

1. Satheesh, S.K.; Moorthy, K.K. Radiative effects of natural aerosols: A review. *Atmos. Environ.* **2005**, *39*, 2089–2110. [CrossRef]
2. Textor, C.; Schulz, M.; Guibert, S.; Kinne, S.; Balkanski, Y.; Bauer, S.; Berntsen, T.; Berglen, T.; Boucher, O.; Chin, M.; et al. Analysis and quantification of the diversities of aerosol life cycles within AeroCom. *Atmos. Chem. Phys.* **2006**, *6*, 1777–1813. [CrossRef]
3. Choobari, O.A.; Zawar-Reza, P.; Sturman, A. The global distribution of mineral dust and its impacts on the climate system: A review. *Atmos. Res.* **2014**, *138*, 152–165. [CrossRef]
4. Kohfeld, K.E.; Harrison, S.P. DIRTMAP: The geological record of dust. *Earth-Sci. Rev.* **2001**, *54*, 81–114. [CrossRef]
5. Gassó, S.; Grassian, V.H.; Miller, R.L. Interactions between mineral dust, climate, and ocean ecosystems. *Elements* **2010**, *6*, 247–252. [CrossRef]
6. Marx, S.K.; Kamber, B.S.; McGowan, H.A.; Petherick, L.M.; McTainsh, G.H.; Stromsoe, N.; Hooper, J.N.; May, J.H. Palaeo-dust records: A window to understanding past environments. *Glob. Planet. Chang.* **2018**, *165*, 13–43. [CrossRef]
7. Thompson, L.G.; Mosley-Thompson, E. Temporal variability of microparticle properties in polar ice sheets. *J. Volcanol. Geotherm. Res.* **1981**, *11*, 11–27. [CrossRef]
8. Petit, J.R.; Briat, M.; Royer, A. Ice age aerosol content from East Antarctic ice core samples and past wind strength. *Nature* **1981**, *293*, 391–394. [CrossRef]
9. De Angelis, M.; Barkoy, N.; Petrov, V. Sources of continental dust over Antarctica during the last glacial cycle. *J. Atmos. Chem.* **1992**, *14*, 233–244. [CrossRef]
10. Delmonte, B.; Paleari, C.I.; Andò, S.; Garzanti, E.; Andersson, P.S.; Petit, J.R.; Crosta, X.; Narcisi, B.; Baroni, C.; Salvatore, M.C.; et al. Causes of dust size variability in central East Antarctica (Dome B): Atmospheric transport from expanded South American sources during Marine Isotope Stage 2. *Quat. Sci. Rev.* **2017**, *168*, 55–68. [CrossRef]
11. Thompson, L.O.; Yao, T.; Davis, M.; Henderson, K.; Mosley-Thompson, E.; Lin, P.N.; Beer, J.; Synal, H.A.; Cole-Dai, J.; Bolzan, J. Tropical climate instability: The last glacial cycle from a Qinghai-Tibetan ice core. *Science* **1997**, *276*, 1821–1825. [CrossRef]
12. Condie, K.C.; Dengate, J.; Cullers, R.L. Behavior of rare earth elements in a paleoweathering profile on granodiorite in the Front Range, Colorado, USA. *Geochim. Cosmochim. Acta* **1995**, *59*, 279–294. [CrossRef]
13. Taylor, S.R.; McLennan, S.M. The geochemical evolution of the continental crust. *Rev. Geophys.* **1995**, *33*, 241–265. [CrossRef]
14. Laveuf, C.; Cornu, S. A review on the potentiality of rare earth elements to trace pedogenetic processes. *Geoderma* **2009**, *154*, 1–12. [CrossRef]
15. Gallet, S.; Jahn, B.M.; Lanoë, B.V.V.; Dia, A.; Rossello, E. Loess geochemistry and its implications for particle origin and composition of the upper continental crust. *Earth Planet. Sci. Lett.* **1998**, *156*, 157–172. [CrossRef]
16. Basile, I.; Grousset, F.E.; Revel, M.; Petit, J.R.; Biscaye, P.E.; Barkov, N.I. Patagonian origin of glacial dust deposited in East Antarctica (Vostok and Dome C) during glacial stages 2, 4 and 6. *Earth Planet. Sci. Lett.* **1997**, *146*, 573–589. [CrossRef]
17. Delmonte, B.; Basile-Doelsch, I.; Petit, J.R.; Maggi, V.; Revel-Rolland, M.; Michard, A.; Jagoutz, E.; Grousset, F. Comparing the Epica and Vostok dust records during the last 220,000 years: Stratigraphical correlation and provenance in glacial periods. *Earth-Sci. Rev.* **2004**, *66*, 63–87. [CrossRef]
18. Delmonte, B.; Petit, J.R.; Andersen, K.K.; Basile-Doelsch, I.; Maggi, V.; Lipenkov, V.Y. Dust size evidence for opposite regional atmospheric circulation changes over east Antarctica during the last climatic transition. *Clim. Dyn.* **2004**, *23*, 427–438. [CrossRef]
19. Delmonte, B.; Andersson, P.S.; Hansson, M.; Schöberg, H.; Petit, J.R.; Basile-Doelsch, I.; Maggi, V. Aeolian dust in East Antarctica (EPICA-Dome C and Vostok): Provenance during glacial ages over the last 800 kyr. *Geophys. Res. Lett.* **2008**, *35*, L07703. [CrossRef]
20. Grousset, F.E.; Biscaye, P.E. Tracing dust sources and transport patterns using Sr, Nd and Pb isotopes. *Chem. Geol.* **2005**, *222*, 149–167. [CrossRef]
21. Yang, J.; Li, G.; Rao, W.; Ji, J. Isotopic evidences for provenance of East Asian Dust. *Atmos. Environ.* **2009**, *43*, 4481–4490. [CrossRef]
22. Lupker, M.; Aciego, S.M.; Bourdon, B.; Schwander, J.; Stocker, T.F. Isotopic tracing (Sr, Nd, U and Hf) of continental and marine aerosols in an 18th century section of the Dye-3 ice core (Greenland). *Earth Planet. Sci. Lett.* **2010**, *295*, 277–286. [CrossRef]
23. Aarons, S.M.; Aciego, S.M.; Arendt, C.A.; Blakowski, M.A.; Steigmeyer, A.; Gabrielli, P.; Sierra-Hernández, M.R.; Beaudon, E.; Delmonte, B.; Baccolo, G.; et al. Dust composition changes from Taylor Glacier (East Antarctica) during the last glacial- interglacial transition: A multi-proxy approach. *Quat. Sci. Rev.* **2017**, *162*, 60–71. [CrossRef]
24. Wolff, E.W.; Fischer, H.; Fundel, F.; Ruth, U.; Twarloh, B.; Littot, G.C.; Mulvaney, R.; Röthlisberger, R.; Angelis, M.D.; Boutron, C.F.; et al. Southern Ocean sea-ice extent, productivity and iron flux over the past eight glacial cycles. *Nature* **2006**, *440*, 491–496. [CrossRef]
25. Aarons, S.M.; Aciego, S.M.; Gabrielli, P.; Delmonte, B.; Koornneef, J.M.; Wegner, A.; Blakowski, M.A. The impact of glacier retreat from the Ross Sea on local climate: Characterization of mineral dust in the Taylor Dome ice core, East Antarctica. *Earth Planet. Sci. Lett.* **2016**, *444*, 34–44. [CrossRef]
26. Biscaye, P.E.; Grousset, F.E.; Revel, M.; Gaast, S.V.D.; Zielinski, G.A.; Vaars, A.; Kukla, G. Asian provenance of glacial dust (stage 2) in the Greenland Ice Sheet Project 2 Ice Core, Summit, Greenland. *J. Geophys. Res. Ocean.* **1997**, *102*, 26765–26781. [CrossRef]
27. Svensson, A.; Biscaye, P.E.; Grousset, F.E. Characterization of late glacial continental dust in the Greenland Ice Core Project ice core. *J. Geophys. Res. Atmos.* **2000**, *105*, 4637–4656. [CrossRef]
28. Bory, A.J.; Biscaye, P.E.; Grousset, F.E. Two distinct seasonal Asian source regions for mineral dust deposited in Greenland (NorthGRIP). *Geophys. Res. Lett.* **2003**, *30*, 1167. [CrossRef]

29. Újvári, G.; Stevens, T.; Svensson, A.; Klötzli, U.S.; Manning, C.; Németh, T.; Kovács, J.; Sweeney, M.R.; Gocke, M.; Wiesenberg, G.L.; et al. Two possible source regions for central Greenland last glacial dust. *Geophys. Res. Lett.* **2015**, *42*, 10399–10408. [CrossRef]
30. Újvári, G.; Stevens, T.; Molnár, M.; Demény, A.; Lambert, F.; Varga, G.; Jull, A.J.T.; Páll-Gergely, B.; Buylaert, J.P.; Kovács, J. Coupled European and Greenland last glacial dust activity driven by North Atlantic climate. *Proc. Natl. Acad. Sci. USA* **2017**, *114*, E10632–E10638. [CrossRef]
31. Újvári, G.; Klötzli, U.; Stevens, T.; Svensson, A.; Ludwig, P.; Vennemann, T.; Gier, S.; Horschinegg, M.; Palcsu, L.; Hippler, D.; et al. Greenland ice core record of last glacial dust sources and atmospheric circulation. *J. Geophys. Res. Atmos.* **2022**, *127*, e2022JD036597. [CrossRef]
32. Han, Y.; Fang, X.; Kang, S.; Wang, H.; Kang, F. Shifts of dust source regions over central Asia and the Tibetan Plateau: Connections with the Arctic oscillation and the westerly jet. *Atmos. Environ.* **2008**, *42*, 2358–2368. [CrossRef]
33. Wei, T.; Dong, Z.; Kang, S.; Rostami, M.; Ulbrich, S.; Shao, Y. Hf-Nd-Sr isotopic fingerprinting for aeolian dust deposited on glaciers in the northeastern Tibetan Plateau region. *Glob. Planet. Chang.* **2019**, *177*, 69–80. [CrossRef]
34. Zdanowicz, C.; Hall, G.; Vaive, J.; Amelin, Y.; Percival, J.; Girard, I.; Biscaye, P.; Bory, A. Asian dustfall in the St. Elias Mountains, Yukon, Canada. *Geochim. Cosmochim. Acta* **2006**, *70*, 3493–3507. [CrossRef]
35. Wu, G.; Zhang, C.; Zhang, X.; Tian, L.; Yao, T. Sr and Nd isotopic composition of dust in Dunde ice core, Northern China: Implications for source tracing and use as an analogue of long-range transported Asian dust. *Earth Planet. Sci. Lett.* **2010**, *299*, 409–416. [CrossRef]
36. Honda, M.; Yabuki, S.; Shimizu, H. Geochemical and isotopic studies of aeolian sediments in China. *Sedimentology* **2004**, *51*, 211–230. [CrossRef]
37. Chen, J.; Li, G.; Yang, J.; Rao, W.; Lu, H.; Balsam, W.; Sun, Y.; Ji, J. Nd and Sr isotopic characteristics of Chinese deserts: Implications for the provenances of Asian dust. *Geochim. Cosmochim. Acta* **2007**, *71*, 3904–3914. [CrossRef]
38. Wei, T.; Brahney, J.; Dong, Z.; Kang, S.; Zong, C.; Guo, J.; Yang, L.; Qin, X. Hf-Nd-Sr Isotopic Composition of the Tibetan Plateau Dust as a Fingerprint for Regional to Hemispherical Transport. *Environ. Sci. Technol.* **2021**, *55*, 10121–10132. [CrossRef]
39. Tripathi, J.K.; Bock, B.; Rajamani, V. Nd and Sr isotope characteristics of Quaternary Indo-Gangetic plain sediments: Source distinctiveness in different geographic regions and its geological significance. *Chem. Geol.* **2013**, *344*, 12–22. [CrossRef]
40. Kumar, A.; Suresh, K.; Rahaman, W. Geochemical characterization of modern aeolian dust over the Northeastern Arabian Sea: Implication for dust transport in the Arabian Sea. *Sci. Total Environ.* **2020**, *729*, 138576. [CrossRef]
41. Jin, Z.; Yu, J.; Wang, S.; Zhang, F.; Shi, Y.; You, C.F. Constraints on water chemistry by chemical weathering in the Lake Qinghai catchment, northeastern Tibetan Plateau (China): Clues from Sr and its isotopic geochemistry. *Hydrogeol. J.* **2009**, *17*, 2037–2048. [CrossRef]
42. Doebbert, A.C.; Johnson, C.M.; Carroll, A.R.; Beard, B.L.; Pietras, J.T.; Carson, M.R.; Norsted, B.; Throckmorton, L.A. Controls on Sr isotopic evolution in lacustrine systems: Eocene green river formation, Wyoming. *Chem. Geol.* **2014**, *380*, 172–189. [CrossRef]
43. Du, Z.; Xiao, C.; Liu, Y.; Wu, G. Geochemical characteristics of insoluble dust as a tracer in an ice core from Miaoergou Glacier, east Tien Shan. *Glob. Planet. Chang.* **2015**, *127*, 12–21. [CrossRef]
44. Xu, J.; Hou, S.; Chen, F.; Ren, J.; Qin, D. Tracing the sources of particles in the East Rongbuk ice core from Mt. Qomolangma. *Chin. Sci. Bull.* **2009**, *54*, 1781–1785. [CrossRef]
45. Kreutz, K.J.; Sholkovitz, E.R. Major element, rare earth element, and sulfur isotopic composition of a high-elevation firn core: Sources and transport of mineral dust in central Asia. *Geochem. Geophys. Geosyst.* **2000**, *1*, 1048. [CrossRef]
46. Wu, G.; Xu, B.; Zhang, C.; Gao, S.; Yao, T. Geochemistry of dust aerosol over the Eastern Pamirs. *Geochim. Cosmochim. Acta* **2009**, *73*, 977–989. [CrossRef]
47. Wu, G.; Zhang, C.; Zhang, X.; Xu, T.; Yan, N.; Gao, S. The environmental implications for dust in high-alpine snow and ice cores in Asian mountains. *Glob. Planet. Chang.* **2015**, *124*, 22–29. [CrossRef]
48. Xu, J.; Yu, G.; Kang, S.; Hou, S.; Zhang, Q.; Ren, J.; Qin, D. Sr-Nd isotope evidence for modern aeolian dust sources in mountain glaciers of western China. *J. Glaciol.* **2012**, *58*, 859–865. [CrossRef]
49. Li, Y.; Li, Z.; Huang, J.; Cozzi, G.; Turetta, C.; Barbante, C.; Xiong, L. Variations of trace elements and rare earth elements (REEs) treated by two different methods for snow-pit samples on the Qinghai-Tibetan Plateau and their implications. *Sci. Cold Arid Reg.* **2018**, *9*, 568–579.
50. Wei, T.; Dong, Z.; Kang, S.; Qin, X.; Guo, Z. Geochemical evidence for sources of surface dust deposited on the Laohugou glacier, Qilian Mountains. *Appl. Geochem.* **2017**, *79*, 1–8. [CrossRef]
51. Prospero, J.M.; Ginoux, P.; Torres, O.; Nicholson, S.E.; Gill, T.E. Environmental characterization of global sources of atmospheric soil dust identified with the Nimbus 7 Total Ozone Mapping Spectrometer (TOMS) absorbing aerosol product. *Rev. Geophys.* **2002**, *40*, 2-1–2-31. [CrossRef]
52. Sun, J. Source regions and formation of the loess sediments on the high mountains regions of northwestern China. *Quat. Res.* **2002**, *58*, 341–351. [CrossRef]
53. Zeng, X.; Xu, X.; Yi, C.; Sun, Y.; Li, J. Extensive glaciations between MIS 8 and MIS 5 on the eastern side of the Guliya ice cap, West Kunlun Mountains. *Quat. Int.* **2021**, *604*, 28–37. [CrossRef]
54. Thompson, L.G.; Yao, T.; Davis, M.E.; Mosley-Thompson, E.; Wu, G.; Porter, S.E.; Xu, B.; Lin, P.N.; Wang, N.; Beaudon, E.; et al. Ice core records of climate variability on the Third Pole with emphasis on the Guliya ice cap, western Kunlun Mountains. *Quat. Sci. Rev.* **2018**, *188*, 1–14. [CrossRef]

55. Sierra-Hernández, M.R.; Gabrielli, P.; Beaudon, E.; Wegner, A.; Thompson, L.G. Atmospheric depositions of natural and anthropogenic trace elements on the Guliya ice cap (northwestern Tibetan Plateau) during the last 340 years. *Atmos. Environ.* **2018**, *176*, 91–102. [CrossRef]
56. Bradley, R.S. Are there optimum sites for global paleotemperature reconstruction? In Proceedings of the Climatic Variations and Forcing Mechanisms of the Last 2000 Years; Jones, P.D., Bradley, R.S., Jouzel, J., Eds.; Springer: Berlin/Heidelberg, Germany, 1996; pp. 603–624.
57. Thompson, L.G. Ice core evidence for climate change in the Tropics: Implications for our future. *Quat. Sci. Rev.* **2000**, *19*, 19–35. [CrossRef]
58. Yao, T.; Shi, Y.; Thompson, L. High resolution record of paleoclimate since the Little Ice Age from the Tibetan ice cores. *Quat. Int.* **1997**, *37*, 19–23. [CrossRef]
59. Herzschuh, U. Palaeo-moisture evolution in monsoonal Central Asia during the last 50,000 years. *Quat. Sci. Rev.* **2006**, *25*, 163–178. [CrossRef]
60. Tison, J.L.; de Angelis, M.; Littot, G.; Wolff, E.; Fischer, H.; Hansson, M.; Bigler, M.; Udisti, R.; Wegner, A.; Jouzel, J.; et al. Retrieving the paleoclimatic signal from the deeper part of the EPICA Dome C ice core. *Cryosphere* **2015**, *9*, 1633–1648. [CrossRef]
61. Vinati, A.; Mahanty, B.; Behera, S. Clay and clay minerals for fluoride removal from water: A state-of-the-art review. *Appl. Clay Sci.* **2015**, *114*, 340–348. [CrossRef]
62. Kamenov, G.D.; Mueller, P.A.; Gilli, A.; Coyner, S.; Nielsen, S. A simple method for rapid, high-precision isotope measurements of small samples with MC-ICP-MS. *Proc. AGU Fall Meet. Abstr.* **2006**, *2006*, V21A-0542.
63. McArthur, J.; Howarth, R.; Shields, G.; Zhou, Y. Strontium isotope stratigraphy. In *Geologic Time Scale 2020*; Elsevier: Amsterdam, The Netherlands, 2020; pp. 211–238.
64. Tanaka, T.; Togashi, S.; Kamioka, H.; Amakawa, H.; Kagami, H.; Hamamoto, T.; Yuhara, M.; Orihashi, Y.; Yoneda, S.; Shimizu, H.; et al. JNdi-1: A neodymium isotopic reference in consistency with LaJolla neodymium. *Chem. Geol.* **2000**, *168*, 279–281. [CrossRef]
65. Jacobsen, S.B.; Wasserburg, G. Sm-Nd isotopic evolution of chondrites. *Earth Planet. Sci. Lett.* **1980**, *50*, 139–155. [CrossRef]
66. Uglietti, C.; Gabrielli, P.; Olesik, J.W.; Lutton, A.; Thompson, L.G. Large variability of trace element mass fractions determined by ICP-SFMS in ice core samples from worldwide high altitude glaciers. *Appl. Geochem.* **2014**, *47*, 109–121. [CrossRef]
67. Sierra-Hernández, M.R.; Beaudon, E.; Gabrielli, P.; Thompson, L. 21st-century Asian air pollution impacts glacier in northwestern Tibet. *Atmos. Chem. Phys.* **2019**, *19*, 15533–15544. [CrossRef]
68. Beaudon, E.; Gabrielli, P.; Sierra-Hernández, M.R.; Wegner, A.; Thompson, L.G. Central Tibetan Plateau atmospheric trace metals contamination: A 500-year record from the Puruogangri ice core. *Sci. Total Environ.* **2017**, *601–602*, 1349–1363. [CrossRef]
69. Wedepohl, K.H. The composition of the continental crust. *Geochim. Cosmochim. Acta* **1995**, *59*, 1217–1232. [CrossRef]
70. Shaw, D.; Reilly, G.; Muysson, J.; Pattenden, G.; Campbell, F. An estimate of the chemical composition of the Canadian Precambrian Shield. *Can. J. Earth Sci.* **1967**, *4*, 829–853. [CrossRef]
71. Shaw, D.M.; Dostal, J.; Keays, R.R. Additional estimates of continental surface Precambrian shield composition in Canada. *Geochim. Cosmochim. Acta* **1976**, *40*, 73–83. [CrossRef]
72. Wu, G.; Yao, T.; Thompson, L.G.; Li, Z. Microparticle record in the Guliya ice core and its comparison with polar records since the last interglacial. *Chin. Sci. Bull.* **2004**, *49*, 607–611. [CrossRef]
73. Qian, W.; Quan, L.; Shi, S. Variations of the dust storm in China and its climatic control. *J. Clim.* **2002**, *15*, 1216–1229. [CrossRef]
74. Zhao, Y.; Huang, A.; Zhu, X.; Zhou, Y.; Huang, Y. The impact of the winter North Atlantic Oscillation on the frequency of spring dust storms over Tarim Basin in northwest China in the past half-century. *Environ. Res. Lett.* **2013**, *8*, 024026. [CrossRef]
75. Zhang, X.Y.; Gong, S.L.; Shen, Z.X.; Mei, F.M.; Xi, X.X.; Liu, L.C.; Zhou, Z.J.; Wang, D.; Wang, Y.Q.; Cheng, Y. Characterization of soil dust aerosol in China and its transport and distribution during 2001 ACE-Asia: 1. Network observations. *J. Geophys. Res. Atmos.* **2003**, *108*, 4261. [CrossRef]
76. Ferrat, M.; Weiss, D.J.; Strekopytov, S.; Dong, S.; Chen, H.; Najorka, J.; Sun, Y.; Gupta, S.; Tada, R.; Sinha, R. Improved provenance tracing of Asian dust sources using rare earth elements and selected trace elements for palaeomonsoon studies on the eastern Tibetan Plateau. *Geochim. Cosmochim. Acta* **2011**, *75*, 6374–6399. [CrossRef]
77. Scheinost, A.; Schwertmann, U. Color Identification of Iron Oxides and Hydroxysulfates. *Soil Sci. Soc. Am. J.* **1999**, *63*, 1463–1471. [CrossRef]
78. Scheinost, A.C. Metal oxides. In *Encyclopedia of Soils in the Environment*; Elsevier Academic Press: Amsterdam, The Netherlands, 2005; pp. 428–438.
79. Jahn, B.M.; Gallet, S.; Han, J. Geochemistry of the Xining, Xifeng and Jixian sections, Loess Plateau of China: Eolian dust provenance and paleosol evolution during the last 140 ka. *Chem. Geol.* **2001**, *178*, 71–94. [CrossRef]
80. Sun, J.; Li, S.H.; Muhs, D.R.; Li, B. Loess sedimentation in Tibet: Provenance, processes, and link with Quaternary glaciations. *Quat. Sci. Rev.* **2007**, *26*, 2265–2280. [CrossRef]
81. Li, C.; Kang, S.; Zhang, Q.; Wang, F. Rare earth elements in the surface sediments of the Yarlung Tsangbo (Upper Brahmaputra River) sediments, southern Tibetan Plateau. *Quat. Int.* **2009**, *208*, 151–157. [CrossRef]
82. Zheng, M. A new type of cesium ore in Tibet. In Proceedings of the 11th New Zealand Geothermal Workshop, Auckland, New Zealand, 8–10 November 1989; pp. 325–326.

83. Gu, L.X.; Zhang, Z.Z.; Wu, C.Z.; Gou, X.Q.; Liao, J.J.; Yang, H. A topaz-and amazonite-bearing leucogranite pluton in eastern Xinjiang, NW China and its zoning. *J. Asian Earth Sci.* **2011**, *42*, 885–902. [CrossRef]
84. Wampler, J.M.; Krogstad, E.J.; Elliott, W.C.; Kahn, B.; Kaplan, D.I. Long-term selective retention of natural Cs and Rb by highly weathered coastal plain soils. *Environ. Sci. Technol.* **2012**, *46*, 3837–3843. [CrossRef]
85. Brunt, R.; Vasak, L.; Griffioen, J. *Fluoride in Groundwater: Probability of Occurrence of Excessive*; Netherlands Institute of Applied Geoscience TNO—National Geological Survey: Utrecht, The Netherlands, 2004.
86. García, M.; Borgnino, L. Chapter 1: Fluoride in the context of the environment. In *Fluorine: Chemistry, Analysis, Function and Effects*; Royal Society of Chemistry: London, UK, 2015; pp. 3–21.
87. Grimaud, D.; Huang, S.; Michard, G.; Zheng, K. Chemical study of geothermal waters of Central Tibet (China). *Geothermics* **1985**, *14*, 35–48. [CrossRef]
88. Zheng, M.; Liu, X. Hydrochemistry of Salt Lakes of the Qinghai-Tibet Plateau, China. *Aquat. Geochem.* **2009**, *15*, 293–320. [CrossRef]
89. Tan, H.; Chen, J.; Rao, W.; Zhang, W.; Zhou, H. Geothermal constraints on enrichment of boron and lithium in salt lakes: An example from a river-salt lake system on the northern slope of the eastern Kunlun Mountains, China. *J. Asian Earth Sci.* **2012**, *51*, 21–29. [CrossRef]
90. Reddy, K.J.; Gloss, S.P. Geochemical speciation as related to the mobility of F, Mo and Se in soil leachates. *Appl. Geochem.* **1993**, *8*, 159–163. [CrossRef]
91. Wichard, T.; Mishra, B.; Myneni, S.C.; Bellenger, J.P.; Kraepiel, A.M. Storage and bioavailability of molybdenum in soils increased by organic matter complexation. *Nat. Geosci.* **2009**, *2*, 625–630. [CrossRef]
92. Chang, Q.; Mishima, T.; Yabuki, S.; Takahashi, Y.; Shimizu, H. Sr and Nd isotope ratios and REE abundances of moraines in the mountain areas surrounding the Taklimakan Desert, NW China. *Geochem. J.* **2000**, *34*, 407–427. [CrossRef]
93. Anders, E.; Grevesse, N. Abundances of the elements: Meteoritic and solar. *Geochim. Cosmochim. Acta* **1989**, *53*, 197–214. [CrossRef]
94. Taylor, S.R.; McLennan, S.M. *The Continental Crust: Its Composition and Evolution*; Blackwell Scientific Pub.: Palo Alto, CA, USA, 1985.
95. Song, Y.; Chen, X.; Qian, L.; Li, C.; Li, Y.; Li, X.; Chang, H.; An, Z. Distribution and composition of loess sediments in the Ili Basin, Central Asia. *Quat. Int.* **2014**, *334–335*, 61–73. [CrossRef]
96. Zan, J.; Fang, X.; Yang, S.; Nie, J.; Li, X. A rock magnetic study of loess from the West Kunlun Mountains. *J. Geophys. Res. Solid Earth* **2010**, *115*, B10101. [CrossRef]
97. Nickel, E. Experimental dissolution of light and heavy minerals in comparison with weathering and intrastratal solution. *Contrib. Sedimentol.* **1973**, *1*, 1–68.
98. Panahi, A.; Young, G.M.; Rainbird, R.H. Behavior of major and trace elements (including REE) during Paleoproterozoic pedogenesis and diagenetic alteration of an Archean granite near Ville Marie, Québec, Canada. *Geochim. Cosmochim. Acta* **2000**, *64*, 2199–2220. [CrossRef]
99. Roy, P.D.; Smykatz-Kloss, W. REE geochemistry of the recent playa sediments from the Thar Desert, India: An implication to playa sediment provenance. *Chem. Der Erde* **2007**, *67*, 55–68. [CrossRef]
100. Delmonte, B.; Andersson, P.S.; Schöberg, H.; Hansson, M.; Petit, J.R.; Delmas, R.; Gaiero, D.M.; Maggi, V.; Frezzotti, M. Geographic provenance of aeolian dust in East Antarctica during Pleistocene glaciations: Preliminary results from Talos Dome and comparison with East Antarctic and new Andean ice core data. *Quat. Sci. Rev.* **2010**, *29*, 256–264. [CrossRef]
101. Chen, J.; Li, G. Geochemical studies on the source region of Asian dust. *Sci. China Earth Sci.* **2011**, *54*, 1279–1301. [CrossRef]
102. Schettler, G.; Romer, R.L.; Qiang, M.; Plessen, B.; Dulski, P. Size-dependent geochemical signatures of Holocene loess deposits from the Hexi Corridor (China). *J. Asian Earth Sci.* **2009**, *35*, 103–136. [CrossRef]
103. Saini, H.S.; Mujtaba, S.A. Depositional history and palaeoclimatic variations at the northeastern fringe of Thar Desert, Haryana plains, India. *Quat. Int.* **2012**, *250*, 37–48. [CrossRef]
104. Inglett, P.; Reddy, K.; Corstanje, R. *Anaerobic Soils*; Elsevier: Amsterdam, The Netherlands, 2005.
105. Zhong, Z.P.; Tian, F.; Roux, S.; Gazitúa, M.C.; Solonenko, N.E.; Li, Y.F.; Davis, M.E.; Etten, J.L.V.; Mosley-Thompson, E.; Rich, V.I.; et al. Glacier ice archives nearly 15,000-year-old microbes and phages. *Microbiome* **2021**, *9*, 160. [CrossRef]